Inorganic Chemistry

pubs.acs.org/IC Article

Introducing of an Unexplored Aza-BODIPY Diradicaloids with 4-(2,6-Di*tert*-butyl)phenoxyl Radicals Located in 1,7-Positions of the Aza-BODIPY Core

Morris Oyelowo, Jacob W. Schaffner, Towhidi Illius Jeaydi, David A. Blank,* Christopher J. Ziegler,* and Victor N. Nemykin*

Cite This: *Inorg. Chem.* 2024, 63, 24008−24021 Read Online

ACCESS | Metrics & More | Article Recommendations | Supporting Information

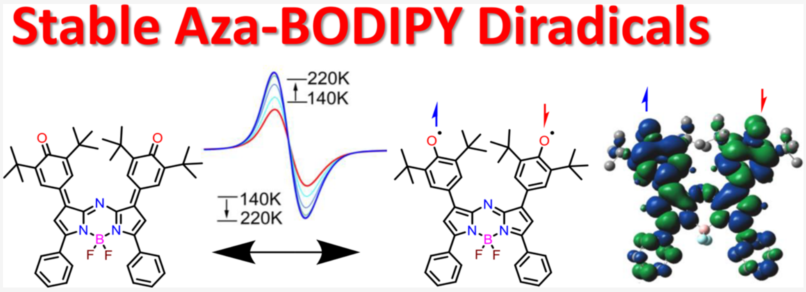

ABSTRACT: We have prepared and characterized two diradicaloid systems **5a** and **5b** that originated from the oxidation of a 1,7-(4-(2,6-di-*tert*-butyl)phenol)-substituted aza-BODIPY core. The aza-BODIPY diradicaloids were characterized by a large array of experimental and computational methods. The diamagnetic closed-shell state was postulated as the ground state in solution and a solid-state with the substantial thermal population originating from both open-shell diradical and open-shell triplet states observed at room temperature. Transient absorption spectroscopy indicates fast (<10 ps) excited state deactivation pathways associated with the target compounds' diradical character in solution at room temperature. Variable-temperature ^{1}H NMR spectra indicate the solvent dependency of the diradical character in **5a** and **5b**. The diradicaloids could be stepwise reduced to the mixed-valence radical-anion and dianion states upon consequent single-electron reductions. Similarly, deprotonated 1,7-(4-(2,6-di-*tert*-butyl)phenol)-substituted aza-BODIPYs can be oxidized to the diradicaloid form. Both mixed-valence and dianionic forms exhibit an intense absorption in the NIR region. Density functional theory (DFT) and time-dependent DFT calculations were used to explain the transformations in the UV−Vis-NIR spectra of all target compounds.

■ INTRODUCTION

4,4-Difluoro-4-bora-3,4-diaza-s-indacene (BODIPY)[1−11] and meso-nitrogen atom substituted BODIPY (aza-BODIPY)[12−17] systems are very popular chromophores that have potential applications as photosensitizers for photodynamic therapy,[18−22] bioimaging agents,[23−27] photosensitizers for solar cells,[28−32] near-IR (NIR) laser agents,[33−37] and solid-state photoelectronic devices,[38−41] including photovoltaic systems,[42−44] organic field effect transistors (OFETs),[45−49] and organic light-emitting diodes (OLEDs).[50−55] The ease of fine-tuning the photophysical and redox properties of this group of compounds[4,5,12] can lead to new applications of this class of materials in spintronics and magnetic memory devices with high storage capacities and fast operation speeds. Organic diradicaloids are a relatively new class of compounds that are thought to provide an alternative pathway for materials useful in spintronics and quantum computing applications.[56−65] A number of Kekule-[66−73] and non-Kekule-based[74−76] diradicaloids have been studied over the past decade. It was shown that the oxygen-centered diradicaloids are significantly more stable under ambient conditions compared to the majority of carbon-centered diradicaloids. The orbital overlap between redox-active fragments and the overall type of the π-system of the chromophore determines whether diradicals exhibit triplet or singlet ground states, although there is still no general guideline developed for predicting such behavior.[56] When applied to the oxygen-centered diradicaloids, oligo-para-phenyl quinones can generally be described as closed-shell resonance structures (diamagnetic), open-shell diradicals, or a superposition of the two.[56] There are only a few Kekulean oxygen-centered species with high diradical character that are stable

Received: October 16, 2024
Revised: November 13, 2024
Accepted: November 18, 2024
Published: November 27, 2024

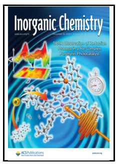

https://doi.org/10.1021/acs.inorgchem.4c04409
Inorg. Chem. 2024, 63, 24008−24021

Scheme 1. Synthesis of Diradicaloids 5a and 5b[a]

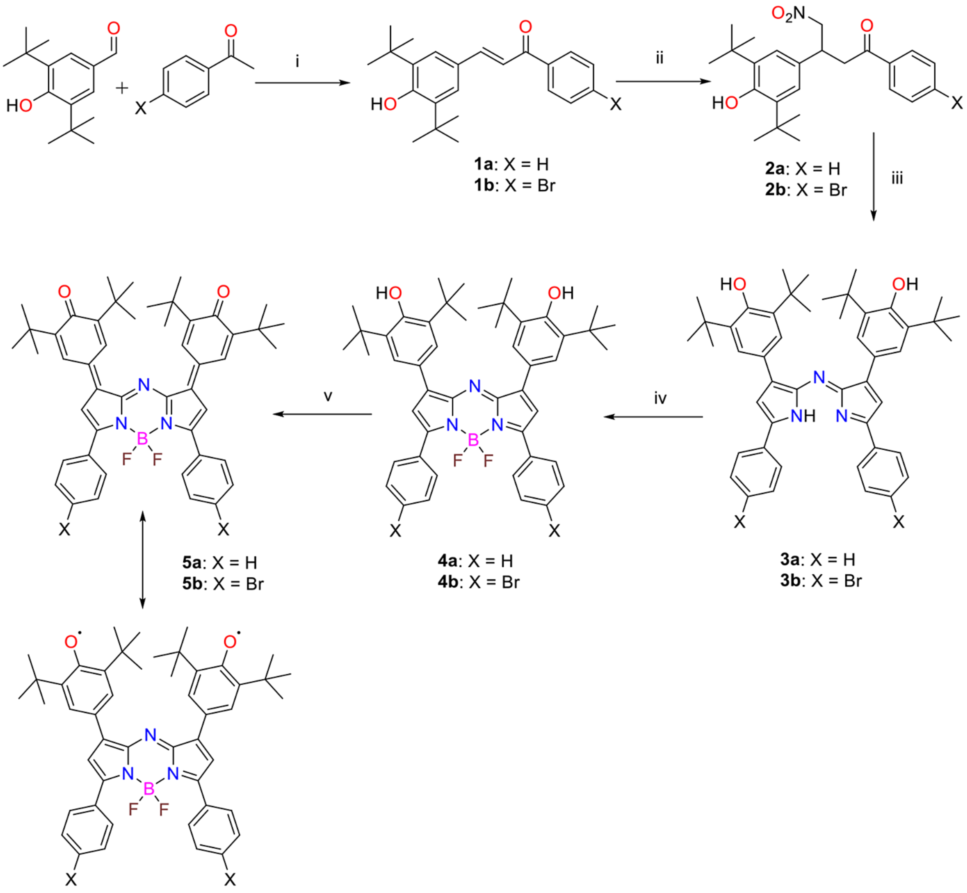

[a]Reagents and conditions: (i) HCl(g), EtOH; (ii) CH_3NO_2, DBU; (iii) NH_4OAc, BuOH; (iv) $BF_3.Et_2O$, DIPEA; and (v) PbO_2.

and persist under laboratory conditions.[56,77−81] The porphyrin-quinones are known to have diamagnetic ground states without any accessible diradical character.[82−84] However, recently, Wu and co-workers reported a single BODIPY-quinone system with diradical properties.[85] In contrast, aza-BODIPYs with diradical character remain unknown. Thus, in this study, we report the first two aza-BODIPY-bridged para-quinoidal systems demonstrating diradical character. We will demonstrate below how the polarity of solvent and phase (i.e., solid-phase versus solution) affect the singlet and triplet diradical character of these compounds (compounds **5a** and **5b**, Scheme 1).

■ RESULTS AND DISCUSSION

Synthesis and Characterization. Compounds **5a** and **5b** were synthesized using a well-established synthetic pathway[12] as shown in Scheme 1. First, an aldol condensation of arylaldehydes and acetophenones gave chalcones **1a** and **1b** in high yields. The chalcones **1a** and **1b** were nitromethylated under standard conditions to form compounds **2a** and **2b** in very high yields. The heterocyclization of the nitromethylated chalcones **2a** and **2b** leads to the formation of aza-DIPYs **3a** and **3b** in 28−45% yield. The BF_2 fragment was then inserted into the aza-DIPYs **3a** and **3b** by using BF_3 etherate in the presence of sterically hindered organic amine to give aza-BODIPYs **4a** and **4b**. Finally, the oxidation of the diphenol-aza-BODIPYs **4a** and **4b** to diradicaloids **5a** and **5b** can be achieved quantitatively by using lead dioxide. Both aza-BODIPY derivatives **4a** and **4b** are stable in solution. However, diradicaloids **5a** and **5b**, although stable for some time in solution, slowly decay over several weeks. Purple (**4a** and **4b**) or olive-green (**5a** and **5b**) compounds can be stored for many months (**4a** and **4b**) or several weeks (**5a** and **5b**) in regular glass vials under ambient conditions. We introduced two bromine atoms in the **2b**−**5b** series to investigate the influence of the heavy-atom effect on the spectroscopic properties of compounds **4b** and **5b** in comparison with **4a** and **5a**.

The influence of the bromine atoms on the UV−vis spectra of **4b** and **5b** as compared with the parent **4a** and **5a** is quite small (Figure 1). The UV−vis spectra of **4a** and **4b** are typical for the tetraaryl-aza-BODIPYs[12] and are dominated by an intense low-energy band observed at 660−670 nm, which follows a lower intensity band at ∼520 nm and several low-intensity transitions observed between 250 and 450 nm. This band shifts to the NIR region (∼800 nm) with a significant reduction in intensity upon oxidation to **5a** and **5b**. The other band in **5a** and **5b** (observed at ∼750 nm) is comparable in intensity with the low-energy transition band observed in these compounds and, according to the TDDFT calculations discussed later, belongs to a different excited state. In addition, prominent bands at ∼555 and ∼388 nm were also observed (Figure 1). The aza-BODIPYs **4a** and **4b** have reasonable fluorescent quantum yields of 19% and 13% respectively, which are lower than those in regular tetraaryl aza-BODIPYs.[11,17,86−88] Such fluorescence quantum yield reduction is expected for BODIPYs and aza-BODIPYs substituted with

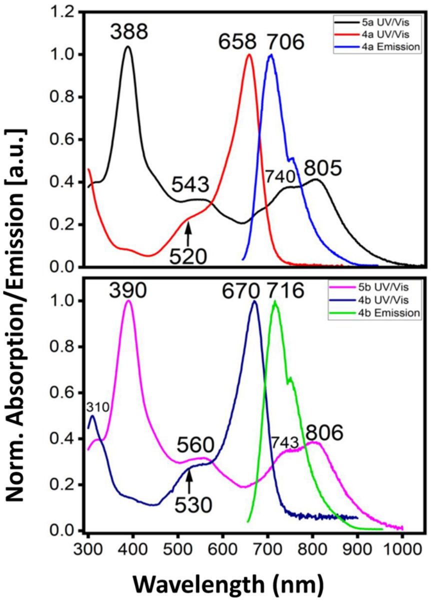

Figure 1. Normalized UV−Vis and fluorescent spectra of **4a**−**b** and **5a**−**b** in DCM.

hydroxy or phenoxy fragments because of the presence of the potential low-energy charge-transfer transition(s) and/or proton-transfer processes in the excited states.[12] Interestingly, two bromine atoms in **4b** do not significantly affect the fluorescence quantum yield in this compound compared to the parent **4a**. The Stokes shifts in **4a** and **4b** are close to 1,000 cm^{-1}, which are within the range (although at the upper border) expected for the aza-BODIPY dyes.[12] The excited state lifetimes for **4a** in DCM and DMF (Table 1) are significantly shorter than those in regular aza-BODIPYs (a few ns), which can be attributed to the potential intramolecular charge- or proton-transfer processes and can be responsible for the lower fluorescence quantum yields in these compounds compared to the standard aza-BODIPYs (Table 1). In contrast, the room-temperature fluorescence in diradicaloids **5a** and **5b** is almost quenched and difficult to measure.

Table 1. Selected Photophysical Properties of the Target Aza-BODIPYs in DCM

compound	λ_{max} (abs) (nm)	ε (10^4 M^{-1} cm^{-1})	λ_{em} (nm)	Φ_f
4a	658	7.02	706	0.19
4b	670	5.87	716	0.13
5a	805	2.70		
5b	807	2.26		

The redox properties of **4a** and **4b** as well as **5a** and **5b** were investigated using electro- (cyclic voltammetry, CV, and differential pulse voltammetry, DPV) and spectroelectrochemical methods. In the case of **4a** and **4b**, two oxidation and four reduction processes were observed in the electrochemical experiments (Figures 2, S1−S3, and Table 2). The oxidation of **4a** and **4b** under spectroelectrochemical conditions results in the formation of diradicaloids **5a** and **5b** and confirms its two-electron, two-proton nature (Figure 3). In particular, the disappearance of the aza-BODIPY transition at 659 (**4a**) or 670 nm (**4b**) and the appearance of lower intensity bands at 739 and 803 nm confirms the formation of **5a** and **5b** under spectroelectrochemical oxidation. Indeed, the final UV−vis spectra of **5a** and **5b** obtained during the oxidation of **4a** and **4b** under chemical and spectroelectrochemical oxidation conditions are identical.

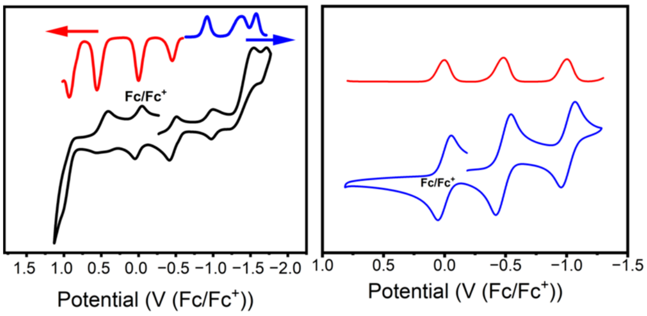

Figure 2. CV and DPV data on **4b** (left) and **5b** (right) in DCM/0.1 M TBAP system.

Table 2. Redox Properties of the Aza-BODIPYs[a]

compound	solvent	Ox$_1$ (V)	Ox$_2$ (V)	Red$_1$ (V)	Red$_2$ (V)	Red$_3$ (V)	Red$_4$ (V)
4a	DCM	0.53	0.88	−0.47	−0.95	−1.40	−1.69
4b	DCM	0.54	0.94	−0.45	−0.94	−1.41	−1.65
5a	DMF			−0.31	−0.90		
	DCM			−0.51	−1.01		
5b	DMF			−0.28	−0.88		
	DCM			−0.48	−1.00		

[a] All redox potentials are listed with respect to Fc/Fc$^+$ oxidation couple (0.1 M TBAP).

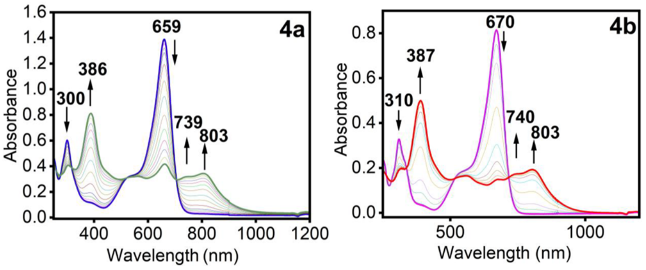

Figure 3. Oxidation of **4a**−**b** into **5a**−**b** under spectroelectrochemical conditions in DCM/0.3 M TBAP system.

The electrochemical experiments on diradicaloids **5a** and **5b** were conducted in relatively low-polarity DCM and polar DMF solvents In both solvents, two reduction processes are observed for both compounds (Figures 2 and S1−S3). The first reduction process in DMF is shifted to a more positive potential for ∼200 mV in both diradicaloids. Taking into consideration the clearly reversible nature of the first and the second reduction processes in DMF and DCM, we conducted spectroelectrochemical stepwise two-electron reduction experiments on **5a** and **5b** (Figure 4 and S4−S7). In both cases and in both solvents, nearly identical spectroscopic changes were observed during stepwise electrolysis. The first reduction process is associated with the growth of bands at ∼950 and ∼1550 nm. These bands disappear during the second reduction process, while intense bands at ∼780 and ∼1200 nm appear in the spectra. The first one-electron reduction process should generate monoradical species [**5a**]$^{-\bullet}$ and [**5b**]$^{-\bullet}$, which have one anionic and one radical terminal oxygen atom (Supporting Information Scheme S1). The low-energy band observed at ∼1500 nm can be assigned as the intervalence

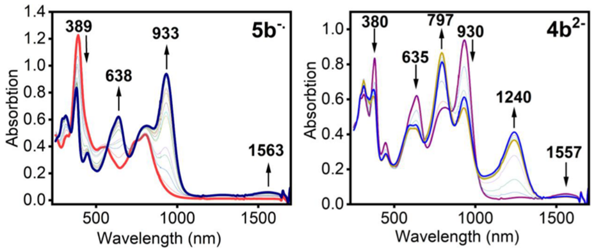

Figure 4. Reduction of **5b** to [**5b**]$^{-\cdot}$ (left) and [**5b**]$^{-\cdot}$ to [**4b**]$^{2-}$ (right) under spectroelectrochemical conditions in DCM/0.3 M TBAP system.

charge-transfer (IVCT) transition expected for the mixed-valence compounds and our TDDFT calculations is in agreement with this assignment. We conducted band deconvolution analysis of the NIR region (~1100−1700 nm) in the UV−vis-NIR spectra of [**5a**]$^{-\cdot}$ and [**5b**]$^{-\cdot}$ and estimated H_{ab} value for these compounds as 374 and 336 cm^{-1}, respectively. These values are typical for class II (weakly coupled) mixed-valence compounds in the Robin-Day classification.[89] The second one-electron reduction process should form diamagnetic [**4a**]$^{2-}$ and [**4b**]$^{2-}$, which have two anionic terminal oxygen atoms and can be viewed as doubly deprotonated **4a** and **4b** compounds (Supporting Information Scheme S1). Indeed, the formation of dianionic [**4a**]$^{2-}$ and [**4b**]$^{2-}$ was further confirmed by the deprotonation of **4a** and **4b** with KOH in MeOH (Figure S8). This experiment also solidifies our assignment for the formation of mixed-valence [**5a**]$^{-\cdot}$ and [**5b**]$^{-\cdot}$ species, which then reduced into [**4a**]$^{2-}$ and [**4b**]$^{2-}$ dianions..

The variable-temperature ^{1}H NMR spectra of **5a** and **5b** were collected in DCM, THF, and DMF (Figures 5 and S42−S46). In DCM and THF as the solvents, the initial broad signals associated with the pyrrolic *β*- and quinone *meta*-protons become narrower with decreasing temperature. It should be noted that quinone *meta*-protons and *tert*-butyl groups in **5a** and **5b** are nonequivalent and give two different signals in their ^{1}H NMR spectra. Such behavior is clearly indicative of the rotational hindrance of the quinoidal fragments in **5a** and **5b**. In the case of DMF as a solvent, the same signals in **5b** at room temperature are significantly broader, while the signals for *meta*-protons in quinone fragments for **5a** are not observable until low temperatures. Thus, VT ^{1}H NMR spectra of **5a** and **5b** are indicative of the presence of the paramagnetic spin density in these compounds. Since NMR line widths reduce with a decrease of the temperature in all solvents (Figures 5 and S42−46), one may suspect the diamagnetic ground state of compounds **5a** and **5b** in the solution. The observed spin density can be associated either with a thermally populated triplet excited state or a thermally populated open-shell diradicaloid state. More interestingly, NMR data in DMF suggest significantly stronger paramagnetism (i.e., the presence of the unpaired electron density at quinoidal fragments in **5a** and **5b**) in this solvent compared to THF and DCM. To the best of our knowledge, this observation is the first report on the solvent-dependent diradicaloid character influenced by solvent polarity.

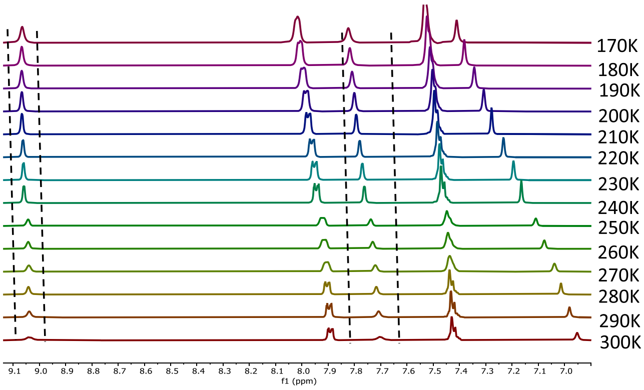

Figure 5. Partial variable-temperature ^{1}H NMR spectrum of **5b** in DMF.

In agreement with the ^{1}H NMR data, we observed room-temperature isotropic EPR signals in **5a** and **5b** in DCM/toluene and the solid-state samples. The g-value of this isotropic signal is close to that of a free electron (Figure 6). The intensity of this signal decreases with the decreasing temperature. Thus, both VT ^{1}H NMR and EPR data suggest a diamagnetic ground state in **5a** and **5b**, and similar behavior was also observed for the BODIPY analog of **5a** and **5b**.[85] The magnetism on **5a** and **5b** was further probed by SQUID measurements (Supporting Information Figures S52−S53). The $\chi_M T$ values between 2 and 320 K gradually increase, which is indicative of the thermal population of the triplet state or open-shell diradicaloid state, which agrees well with the EPR and ^{1}H NMR data. The magnetometry data fit well to the Bleaney−Bowers equation giving $\Delta E_{S\text{-}T}$ values of 1.107 kcal/mol for **5a** and 1.1072 kcal/mol for **5b**), which are virtually identical (Supporting Information Figures S52−S53). Again, the values of the singlet−triplet gap have a reasonable magnitude of the interaction between two centers with partial radical character.[53] In more polar THF and DMF, no EPR signal was observed between room temperature and the freezing point of the solvent. This behavior is not surprising as both THF and DMF strongly absorb microwave irradiation in the liquid phase when the regular EPR cavity is used in the experiment.[90] The lack of $M_s \pm 2$ EPR signal in the EPR spectra at 2 K for frozen DMF solutions of **5a** and **5b** (and the presence of the isotropic signal at this temperature) is indicative of the diamagnetic ground state with open-shell diradicaloid singlet state being in close proximity.

The X-ray structures of **3a** and **5a** (as DMF solvate) were obtained and shown in Figure 7. The structure of **5a** was elucidated at room temperature as well as −50 and −173 °C. In particular, we focused on the temperature dependency for C═O and C═C bonds in quinoidal fragments. First, similar to the recently published structure of BODIPY-quinone-based diradicaloid,[85] the torsion angles between two quinone fragments and the BODIPY core in **5a** are slightly different at all three temperatures (Table 3). The C═O bond distances are slightly longer than those expected for classic carbonyl groups and quinones as well as those observed for the BODIPY analogue of **5a**. However, they all have double-bond rather than single-bond in character. The C−C bond distances in quinoidal fragment alternate; however, again, C═C bond distances are slightly longer than those expected for quinones. The C═C bond distance between two carbon atoms that connect quinoidal fragment with aza-BODIPY core in **5a** (~1.4 Å) is significantly shorter than that in **3a** (~1.47 Å). There were no systematic trends observed for C−C and C═C bond distances in **5a** as a function of temperature (Table 3).

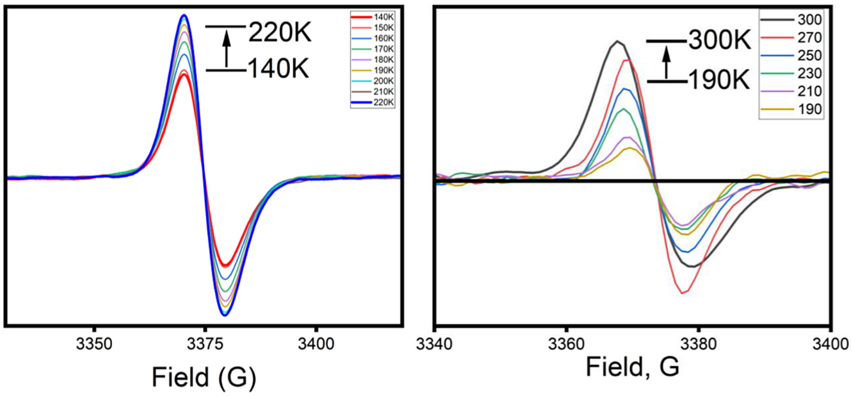

Figure 6. Variable-temperature EPR spectra of **5a** in a solid state (left) and DCM/toluene solution (right).

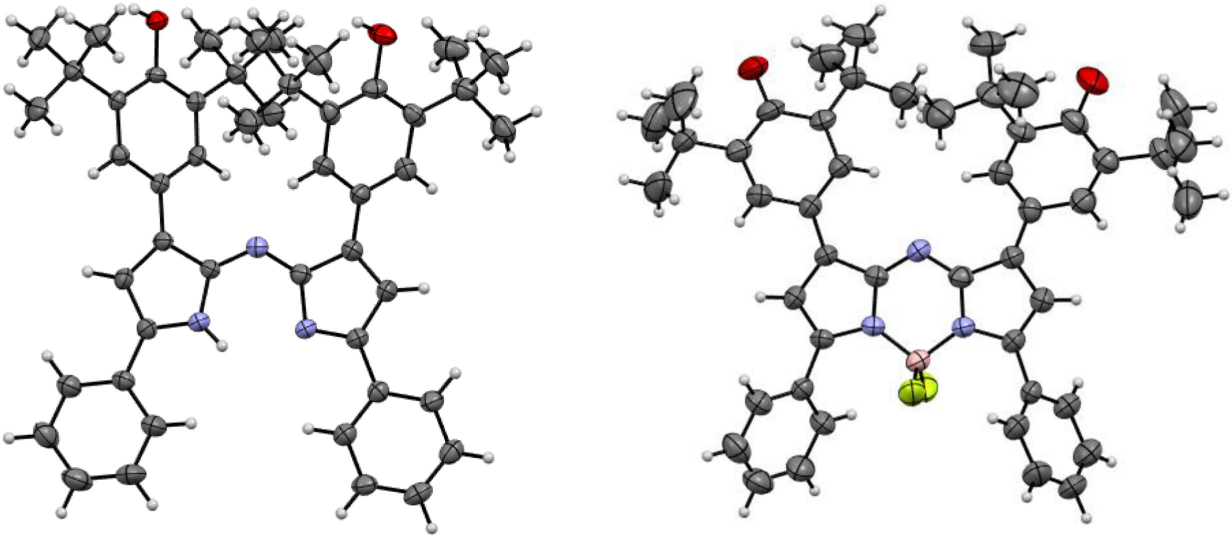

Figure 7. X-ray crystal structures of **3a** (left) and **5a** (right) at 50% thermal ellipsoids.

However, observed bond distances imply some diradical character in this compound. In agreement with this assignment, a clear carbonyl C═O peak is present in the IR spectra of **5a** and **5b** (Figure S10).

Transient absorption spectra of **4a**, **5a**, and **5b** were collected in DCM and DMF (Figure 8 and S47−S51). No significant differences between the two solvents were observed for the **5a** and **5b**, which is, apparently, indicative of the lack of the influence of a bromine atom at *para*-position of the phenyl substituent on the expected intersystem crossing process. The excited state lifetime for **4a** was found to be solvent-dependent (Table 4) and was significantly shorter than typical aza-BODIPY and BODIPY compounds[12] probably because of the potential proton-transfer or intramolecular charge-transfer processes in these compounds. The excited state lifetimes of **4a** in polar DMF was less than half of that in less polar DCM, and it was the only sample that exhibited a biexponential decay indicating more complicated relaxation. The excited state lifetimes for diradicaloids **5a** and **5b** are an order of magnitude shorter (Table 4) than **4a**, and are similar to known diradicals with thermally populated or ground-state paramagnetic character.[56] The excited state lifetimes of **5a** and **5b** are only weakly solvent dependent, with a slightly shorter lifetime in DMF. An order of magnitude reduction of the excited states lifetimes in **5a** and **5b** at room temperature compared to those observed in **4a** is consistent with non-negligible diradical character in **5a** and **5b,** in agreement with the other experiments discussed above.

DFT and TDDFT Calculations. Taking into consideration the close similarities in spectroscopy between brominated and nonbrominated series of compounds, we only conducted extensive DFT and TDDFT calculations on **4a**, **5a**, [**5a**]$^{-\bullet}$, and [**4a**]$^{2-}$. In the case of **4a** and [**4a**]$^{2-}$, only diamagnetic ground states were considered. Similarly, only the doublet ground state was considered for [**5a**]$^{-\bullet}$. Three states were considered for **5a**: (i) diamagnetic closed-shell singlet (**5aDS**), (ii) open-shell singlet diradicaloid (**5aOS**), and (iii) open-shell triplet (**5aTS**). The DFT-predicted energy diagrams are shown in Figure 9 and Supporting Information Figure S53 and the frontier orbital compositions are depicted in the Supporting Information Figures S50−S52 and S60, and Table S2. Independent of the used exchange-correlation functional (Table 5), the triplet state was found to be ∼5 to 8 kcal/mol above the open- and closed-shell singlet states. Both the singlet state and the open-shell diradical state in **5a** were found in very close energies to each other when global hybrid functionals were used (Table 5). However, range-separated functionals predict the open-shell diradical ground stat at ∼1 to 2 kcal/mol below the closed-state state. The DFT calculations for open-shell systems are indicative of a large delocalization of the spin density over the whole molecule with predicted spin density at the oxygen atoms ranging only between 0.06 and 0.22e$^-$ depending on the

Table 3. Selected Bond Distances Observed in the Variable-Temperature XRD Experiments for **5a**

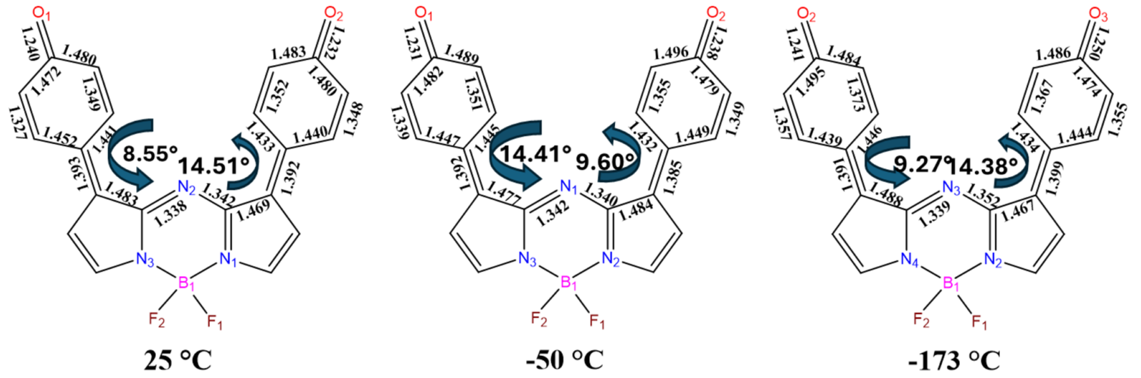

bond distance/T	25 °C	−50 °C	−173 °C
O1−C1	1.240(5)	1.231(4)	1.241(8)
O2−C12	1.232(4)	1.238(4)	1.250(8)
C1−C2	1.472(6)	1.482(5)	1.495(9)
C1−C6	1.480(5)	1.489(5)	1.484(9)
C2−C3	1.372(5)	1.339(5)	1.357(9)
C3−C4	1.452(5)	1.447(5)	1.439(9)
C4−C5	1.441(5)	1.445(5)	1.446(9)
C4−C7	1.393(5)	1.392(5)	1.391(9)
C5−C6	1.349(5)	1.351(5)	1.373(9)
C8−C9	1.392(5)	1.385(5)	1.399(9)
C9−C10	1.433(5)	1.432(5)	1.434(9)
C9−C14	1.440(5)	1.449(5)	1.444(9)
C10−C11	1.352(5)	1.355(5)	1.367(8)
C11−C12	1.483(5)	1.496(5)	1.486(9)
C12−C13	1.480(6)	1.479(5)	1.474(9)
C13−C14	1.348(5)	1.349(5)	1.355(9)
torsion angle TS1	8.55°	14.41°	9.27°
torsion angle TS2	14.51°	9.60°	14.36°

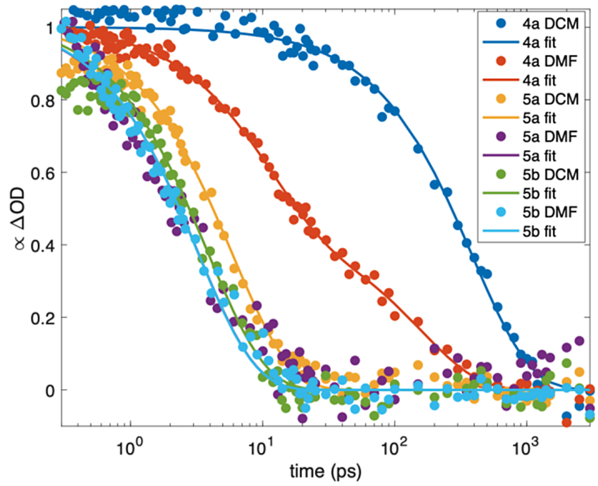

Figure 8. Excited state absorption following excitation at 531 nm. Fitted time constants and the wavelengths of the probe are presented in Table 4. Full ΔOD spectra are presented in Figure S47.

used exchange-correlation functional (Table 5 and Figure 9). The DFT-predicted diradical character (y_0) for **5aOS** was calculated using procedures reported earlier[56,90,91] and values are summarized for several exchange-correlation functionals in Table 5. Again, a clear diradicaloid nature can be seen for **5a**, which is in agreement with the experimental data.

Table 4. Excited State Lifetimes Following Excitation at 531 nm[b]

compound	solvent	probe range (nm)	lifetime (ps)
4a	DCM	420−460	388 ± 10
4a[a]	DMF	500−560	10.1 ± 0.6 (55.8%) 158 ± 11 (44.2%)
5a	DCM	480−540	5.9 ± 0.2
5a	DMF	440−500	3.2 ± 0.2
5b	DCM	500−560	3.9 ± 0.2
5b	DMF	500−560	3.2 ± 0.1

[a] **4a** in DMF could not be well fitted by a single exponential decay and required the sum of two exponential decay components with the indicated relative contributions. [b] These were all determined by single exponential decay fits to transient absorption from the excited state in the indicated wavelength range. The data and fits are presented in Figure 8, and the full frequency pump-probe spectra are presented in Figure S47.

The HOMO and the LUMO in **4a** and $[\mathbf{4a}]^{2-}$ are typical for BODIPYs and aza-BODIPYs (Supporting Information Figure S60).[12] The HOMO has a large contribution from the pyrrolic α- and β-carbon atoms, while the LUMO has a large contribution from the nitrogen atoms. Two-electron oxidation of **4a** to **5a** result is the electronic structure close to that discussed earlier for MB-DIPYs.[92−96] Indeed, the HOMO in open- and closed-shell singlets of **5a** has a significant contribution from the nitrogen atoms, while the LUMO has a significant contribution from the pyrrolic α- and β-carbon

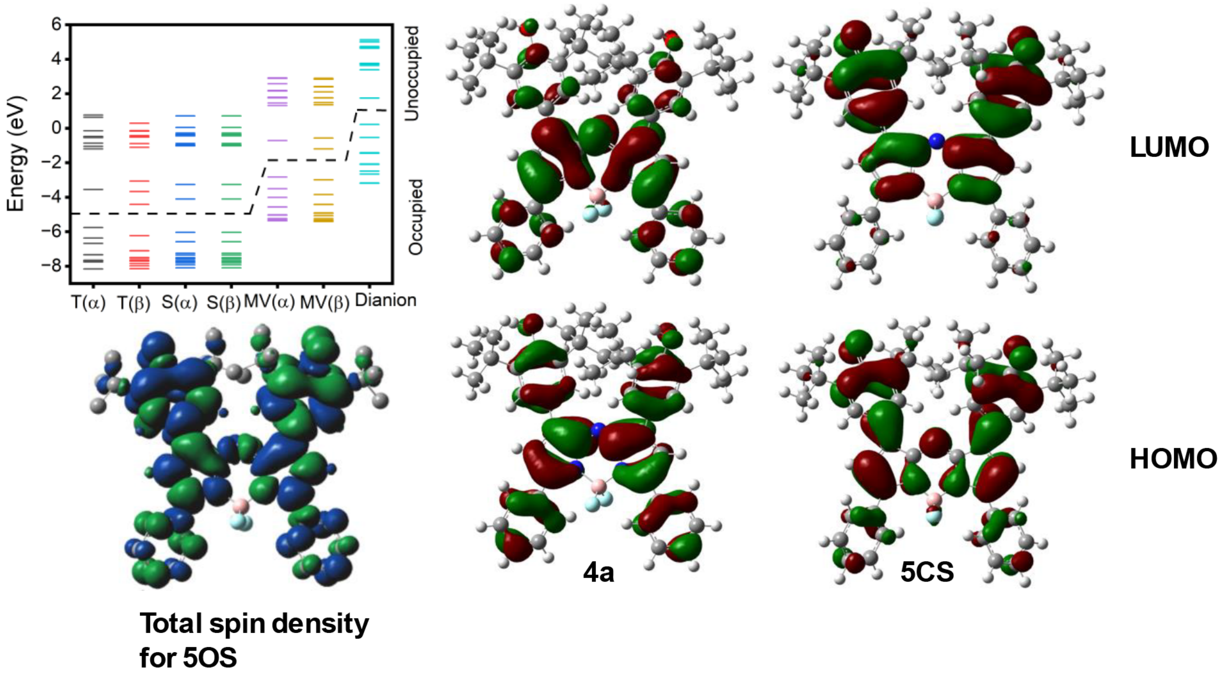

Figure 9. DFT-predicted (M06 exchange-correlation functional) energy diagram (top left), total spin density for **5OS** (bottom left), and HOMO/LUMO pairs for **4a** and **5DS**. (T = 5TS; S = 5OS; MV = $[\mathbf{5a}]^{-\cdot}$; dianion = $[\mathbf{4a}]^{2-}$)

Table 5. DFT-Predicted Relative Energies (kcal/mol), Spin Densities at the Oxygen Atoms, and Diradical Character Coefficients (y_0 for 5OS Only) for 5DS, 5OS, and 5TS

ECF[a]	5DS	5OS[b]	5TS[b]	y_0
TPSSh	0.005	0 (0.06)	4.99 (0.29)	0.054
M06	0.003	0 (0.03)	6.42 (0.27)	0.028
CAM-B3LYP	1.13	0 (0.21)	6.11 (0.31)	0.135
wB97X	1.76	0 (0.22)	7.97 (0.31)	0.185

[a] ECF = exchange-correlation functional. [b] Spin densities at the oxygen atoms are provided in parentheses.

atoms. More interesting, the HOMO−2 and HOMO−3 in **5OS** and **5DS** are localized on the quinone fragments, and the HOMO−4 and HOMO−5 are localized on the phenyl substituents, which opens a pathway for potential interligand charge-transfer (ILCT) like transitions in these systems. In contrast, the DFT-predicted HOMO and LUMO in **5TS** resemble those in normal aza-BODIPYs and BODIPYs (Supporting Information Figure S60).

TDDFT calculations for all compounds are in good agreement with the experimental data (Figure 10 and Supporting Information Figures S54−S59). In particular, they correctly predict the red shift of the most intense low-energy peak in $\mathbf{4a}/[\mathbf{5a}]^{-\cdot}/[\mathbf{4a}]^{2-}$ series, the energy of the IVCT band in the mixed-valence $[\mathbf{5a}]^{-\cdot}$, and the red shift as well as the significant drop in intensity of the aza-BODIPY's low-energy band upon oxidation of **4a** to **5a**. Interestingly, the TDDFT-predicted UV−vis spectra for **5OS**, **5TS**, and **5DS** are fairly similar, which probably reflects their close energies and electronic structures (Supporting Information Figures S54−S59).

In the case of parent **4a**, the lowest energy transition belongs to almost pure HOMO → LUMO single-electron excitation and this is usual for BODIPY and aza-BODIPY systems.[12] The HOMO → LUMO single-electron excitation has small phenol → aza-BODIPY core interligand charge-transfer (ILCT) character, which might be responsible for the decreased fluorescence quantum yield and shorter than usual excited state lifetime in **4a** and **4b** (Figures S47−S51 and Table 4, and Supporting Information Table S1). TDDFT calculations also predicted two unusual excited states around 500 nm (excited states 2 and 3, Supporting Information Table S1). These are dominated by the HOMO−1 → LUMO and HOMO−2 → LUMO single-electron transitions, respectively, and have substantial phenol → aza-BODIPY core ILCT character (Supporting Information Figure S54 and Table S1). Deprotonation of the **4a** and **4b** increases the donor ability of the phenol fragments and thus, it was not surprising to see that the ILCT process contributes more to the first and second excited states of $[\mathbf{4a}]^{2-}$ (Figure 10, Supporting Information Figure S57, and Table S1). Indeed, these are dominated by the HOMO → LUMO and HOMO−1 → LUMO single-electron transitions that have a significant phenolate → aza-BODIPY core ILCT character. Single-electron reduction of **5a** or **5b** leads to the formation of the mixed-valence $[\mathbf{5a}]^{-\cdot}$ or $[\mathbf{5b}]^{-\cdot}$ systems with characteristic IVCT band observed ~1550 nm. TDDFT calculations confirm that this excited state has substantial IVCT character (excited state 1 predicted at ~1400 nm; Supporting Information Table S1 and Figure S56). According to TDDFT calculations, in the low-energy region, the UV−vis spectrum of $[\mathbf{5a}]^{-\cdot}$ is dominated by the excited states 3 (870 nm; f = 0.41) and 8 (568 nm; f = 0.40). Both excited states have substantial ILCT (phenoxy → aza-BODIPY core) character (Supporting Information Figure S60 and Table S3). In the case of the lowest-energy **5OS** diradicaloid, TDDFT calculations predict that the UV−vis spectrum should be dominated by three excited states (Supporting Information Table S1 and Figure 10). The lowest energy excited state of high intensity (836 nm; f = 0.330) is dominated by the $\text{HOMO}_{\alpha,\beta}$ → $\text{LUMO}_{\alpha,\beta}$ single-electron transitions and has a small ILCT contribution. The second excited state (excited state 8 predicted at 571 nm; f = 0.374) is dominated by the

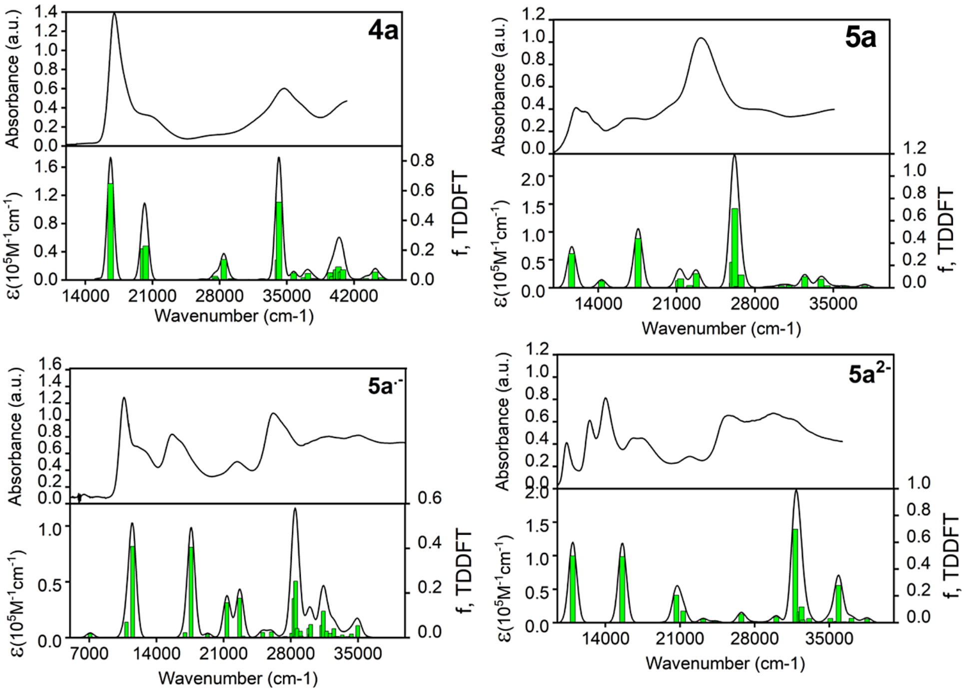

Figure 10. Experimental versus TDDFT-predicted (M06 exchange-correlation functional) UV−vis spectra of **4a**, **5a**, [**5a**]$^{-\cdot}$, and [**4a**]$^{2-}$.

$\mathrm{HOMO}_{\alpha,\beta}$ → $\mathrm{LUMO+1}_{\alpha,\beta}$ (53%) and $\mathrm{HOMO-1}_{\alpha,\beta}$ → $\mathrm{LUMO}_{\alpha,\beta}$ (18%) single-electron transitions. The third one has a significantly more complex structure and was predicted at 387 nm (f = 0.603; Figure 10). In addition, there are two weaker transitions between 800 and 600 nm predicted by TDDFT calculations. The first one (predicted at 661 nm) is dominated by the $\mathrm{HOMO-1}_{\alpha,\beta}$ → $\mathrm{LUMO}_{\alpha,\beta}$ (73%) single-electron transitions. The second one (predicted at 647 nm) is dominated by the $\mathrm{HOMO}_{\alpha,\beta}$ → $\mathrm{LUMO+1}_{\alpha,\beta}$ (58%) and $\mathrm{HOMO-1}_{\alpha,\beta}$ → $\mathrm{LUMO}_{\alpha,\beta}$ (37%) single-electron transitions. For **5DS** species, TDDFT predicts very similar excited states. In particular, according to TDDFT data, the low-energy envelope (500−900 nm) should be dominated by two excited states. The first state (excited state 1, f = 0.306) is predicted at 860 nm and is pure HOMO → LUMO transition and the second one (excited state 5, f = 0.4397) is predicted at 570 nm and is dominated by the HOMO → LUMO+1 single-electron excitation. Two weak transitions were also predicted in this region. The first one (669 nm, f = 0.06) is dominated by the HOMO−1 → LUMO single-electron excitations and the second transition (622 nm, f = 0.001) is dominated by the HOMO−2 → LUMO single-electron excitations. Finally, similar to the TDDFT data on **5OS**, TDDFT calculations on **5DS** predict a very strong transition located at 382 nm (f = 0.708). This excited state is predominantly formed by the HOMO−11 → LUMO single-electron excitations. Overall, TDDFT predictions suggest that the low-energy region (600−900 nm) in the UV−vis-NIR spectra of **5a** and **5b** has two closely spaced bands originating from two different excited states.

■ CONCLUSIONS

In this paper, we report the preparation and characterization of two diradicaloid systems (**5a** and **5b**) that originated from the oxidation of the 1,7-(4-(2,6-di-*tert*-butyl)phenol)-substituted aza-BODIPY cores **4a** and **4b**. The aza-BODIPY diradicaloids were characterized by a large array of experimental and computational methods. The diamagnetic closed-shell state was postulated as the ground state in solution and a solid state with the substantial thermal population originating from both open-shell diradical and open-shell triplet state observed at room temperature. Transient absorption spectroscopy indicates fast (∼3 to 6 ps) excited state deactivation pathways associated with the target compounds' diradical character in solution at room temperature. The presence of two bromine atoms in **5b** does not influence any photophysical properties in the phenolic or diradicaloid systems to a significant extent. The diradicaloids **5a** and **5b** could be stepwise reduced to the mixed-valence radical-anions [**5a**]$^{-\cdot}$ and [**5b**]$^{-\cdot}$, respectively, and dianion states [**4a**]$^{2-}$ and [**4b**]$^{2-}$ upon consequent single-electron reductions. Similarly, deprotonated 1,7-(4-(2,6-di-*tert*-butyl)phenol)-substituted aza-BODIPYs [**4a**]$^{2-}$ and [**4b**]$^{2-}$ can be oxidized to the diradicaloid forms **5a** and **5b** under spectroelectrochemical conditions. Both mixed-valence and dianionic forms have an intense absorption in the NIR region. Density Functional Theory (DFT) and time-dependent DFT (TDDFT) calculations were used to explain the transformations in the UV−vis−NIR spectra of all target compounds.

■ EXPERIMENTAL SECTION

General. All solvents were purchased from commercial sources and purified using standard procedures. All glassware was rigorously dried overnight at 160 °C and cooled under vacuum prior to use. All reagents and starting materials were purchased from commercial vendors and used without further purification. Column chromatography was performed on silica gel (Dynamic Adsorbents, Inc., 63−200 μm). Deuterated solvents were purchased from Cambridge Isotope Laboratories and used as received.

Electrochemistry. Cyclic voltammetry measurements were made using a three-electrode system consisting of a glassy carbon or platinum working electrode, a platinum auxiliary electrode, and an Ag/AgCl wire pseudo reference electrode. Ferrocene (Fc) was used as an internal standard for the studied compounds, and the reported potentials were corrected to the Fc/Fc^{+} couple. For consistency, all potentials and figures in this work are reported vs the Fc/Fc$^+$ redox couple. All electrochemical experiments were conducted in either dichloromethane (DCM) or *N*,*N*-dimethylformamide (DMF) and 0.1 M tetrabutylammonium perchlorate (TBAP) as electrolyte.

Spectroelectrochemistry. Spectroelectrochemical experiments were performed using a Jasco V-770 UV−vis−NIR spectrophotometer in tandem with a CH Instruments electrochemical analyzer, which was operated using the bulk electrolysis mode. The data were collected using a custom-made 1 mm cell, a platinum mesh working electrode, a platinum auxiliary electrode, and Ag/AgCl wire pseudo reference electrode. Spectroelectrochemical solutions consisted of 0.3 M solutions of TBAP in DCM and DMF.

NMR. NMR spectra were recorded on a 500 MHz Bruker III spectrometer. All chemical shifts (δ) are listed in parts per million (ppm) and are referenced to solvent. Spectra are referenced internally due to residual proton solvent resonances. Variable-temperature ^{1}H NMR spectra were collected in DCM-d_2, THF-d_8, or DMF-d_7 solutions in 10- or 20-degree increments.

Magnetometry. Magnetic studies were carried out using a 7-T Quantum Design SQUID magnetometer at the applied magnetic fields H = 1000, 3000, and 5000 Oe and at temperature T = 2−320 K. The empty plastic capsule exhibited diamagnetism, and its magnetic moment was measured for correction. For both samples in powder form, primary correction for diamagnetism is implemented by point-by-point background subtraction, together with Pascal constants correction. KaleidaGraph software[97] was used for data analysis.

EPR. EPR spectra were recorded on a Bruker ELEXSYS E-500 instrument at the X-band frequency (9,82 GHz). DPPH (g = 2.0036) was used as the standard for field and frequency calibration.

Single-Crystal X-ray Crystallographic Analysis. Single crystals of 3a were obtained by slow cooling of a hot butanol solution. Single crystals of 5a were obtained by slow evaporation of the saturated DMF solution. Crystalline samples were mounted on a 150 mm MiTeGen Dual-Thickness MicroMount using Paratone N oil (Hampton). X-ray diffraction experiment on 3a was conducted at 150 K, while for 5a data were collected at 150, 223, and 298 K. In the case of the room-temperature experiment, the single crystal was glued to the MiTeGen mesh using epoxy glue. Diffraction data was collected using a Bruker Smart Apex II single crystal diffractometer with a TRIUMPH monochromated Mo Kα radiation (λ = 0.71073 Å) source with a crystal-to-detector distance of 50 mm, using a series of θ and ω scans in 0.50° oscillations. The data was processed and corrected for Lorentz and polarization effects and an empirical absorption correction was applied, using the Bruker Apex II software suite. The structures were solved with ShelxS,[98] and subsequent refinements were performed using the SHELXTL crystallographic software package of Bruker-AXS.[99] The coordinates and anisotropic displacement parameters for the non-hydrogen atoms were refined. Hydrogen atoms were placed in idealized geometric positions and linked to their respective carbon atoms using a riding model during refinement. Platon SQUEEZE algorithm[100] was used to remove the electron density associated with the DMF solvent molecule for the room-temperature data set of 5a because of the severe disorder of DMF molecule at this temperature. Diagrams were prepared using MERCURY.[101] Additional crystallographic information can be found in CCDC 2388285 (3a), 2388288 (5a, 150 K), 2388287 (5a, 223 K), and 2388286 (5a, 298 K), respectively.

Determination of Fluorescence Quantum Yield. All fluorescence spectra were corrected for apparatus response. Quartz cuvettes with an optical path of 1 cm were used. The sample concentrations were chosen to obtain a maximum absorbance between 0.3 and 1.0 for UV spectra and between 0.05 and 0.1 at excitation wavelength for quantum yield measurements. Relative quantum yields were obtained by comparing the areas under the corrected emission spectrum. All measurements were performed in chloroform and DCM at 298 K. 1,3,5,7-Tetraphenyl-aza-BODIPY (Φ_F = 0.34 in $CHCl_3$, λ_{ex} = 650 nm) was used as a reference for all measurements. In all quantum yield determinations, correction for the solvent refractive index (η) was applied [$CHCl_3$: η = 1.4458, DCM: η = 1.442]. The following equation was used to calculate the quantum yield of the sample:

$$\Phi_F(X) = \Phi_{ref}(Grad_X/Grad_{ref})(\eta_X{}^2/\eta_{ref}{}^2)$$

Of which indices X and ref stand for the studied compounds (**4a** and **4b**) and the reference compound, respectively, Φ_F is the quantum yield, Grad is the gradient of the linear graph between the integrated fluorescence intensity versus absorbance at the excitation wavelength, and η is the refraction index of the solvent in which the measure is performed.

Computational Methods. All computations were performed using Gaussian 16 software[102] running under Windows or UNIX OS. Molecular orbital contributions were compiled from single-point calculations using the QMForge program.[103] In DFT calculations, the TPSSh[104,105] (10% of Hartree−Fock exchange) and M06[106] (27% of Hartree−Fock exchange) hybrid exchange correlation functionals as well as range-separated CAM-B3LYP[107] and wB97X[108] exchange-correlation functionals were used for geometry optimization. In all calculations, 6-311G(d) basis set was employed.[109] In the case of modeling compound 5a, three spin states were considered. In the first one (5CS), a molecule of 5a was treated as a closed-shell singlet. In the case of 5OS, a molecule of 5a was treated as an open-shell diradicaloid. Stable = opt keyword was used to ensure the correct diradicaloid character of the initial guess and the final wave function. In the case of 5TS, triplet state was used in calculations. Frequencies were calculated for each geometry optimization to ensure the energy minimum. DFT calculations for 4a, 5CS, 5OS, and 5TS converged to C_2 symmetry, which was used in the single-point and TDDFT calculations. In all TDDFT calculations, the lowest 40 excited states were calculated to cover experimentally observed transitions in the UV−visible region. Diradical character in 5OS was further probed using TPSSh, CAM-B3LYP, M06, and wB97X[109] exchange-correlation functionals and the Natural Population Analysis (NPA) algorithm.

Transient Spectroscopy. *Pump−Probe Experimental Setup.* A home-built, regeneratively amplified Ti:sapphire laser system produced ∼80 fs, 1W, 810 nm pulse at a repetition of 1 kHz. This was divided with 90% of the energy used to pump a noncollinear optical parametric amplifier (NOPA) for excitation pulses (the pump centered at 531 nm), and the rest was used to generate the probe by focusing into a 2 mm sapphire to create a continuum spanning 420−750 nm. Pump pulses were modulated at half the repetition rate of the laser by a mechanical chopper. The pump power at the sample ranged from 75 to 110 μW. The pump was polarized to 54.7° relative to the probe to minimize anisotropic dynamics. The time delay between the pump and the probe was controlled by a mechanical delay stage (Newport UTM150PP.1). The two beams were focused and crossed in a 1 mm path length sample cuvette. After the sample, the probe beam was collimated, focused on a monochromator (Princeton Instruments SP2150i monochromator 150 lines/mm, 500 nm blaze), and detected on a 256-pixel linear diode array (Hamamatsu S3902−256Q). Measuring the probe beam with and without the pump for each sequential pair of laser pulses provided the change in optical density, ΔOD, on a shot-to-shot basis. Typical spectra represent an average of 10,000 pulse pairs. Samples were dissolved in DCM or DMF and continuously flowed at a rate of 3.5 mL/min. The samples were excited at 531 nm, where they were diluted to have an optical density of ∼0.1. Absorption spectra were taken before and after pump−probe data collection. Only minor changes were observed before and after the pump−probe experiments for all samples except 5a and 5b in DMF, suggesting minimal photodegradation during these experiments. For 5a and 5b in DMF, there were significant changes in the absorption and ΔOD spectrum that developed over the course of collecting 25 repeated scans of the time delays. As a result, only the first six scans were used, where no changes were evident within the available signal-to-noise. Samples were saturated with N_2 immediately prior to all measurements.

Pump−Probe Fitting. The pump−probe data was fitted as a function of time at wavelengths corresponding to excited state absorption (see Figure S47) and represent the excited state lifetime. All samples were well fitted with a single exponential decay except **4a** in DMF, which was fitted with the sum of two exponential decays. The optimized fitting parameters are presented in Table 4. All fits were convoluted with an 83 fs Gaussian instrument response.

Synthetic Procedures. *Synthesis of (E)-3-(3,5-Ditert-butyl-4-hydroxyphenyl)-1-phenylprop-2-en-1-one (**1a**) and (E)-1-(4-Bromophenyl)-3-(3,5-ditert-butyl-4-hydroxyphenyl)-1-phenylprop-2-en-1-one (**1b**).* Both chalcones **1a** and **1b** were prepared as previously reported.[110] 3,5-di-*tert*-4-hydroxylbenzaldehyde (25 mmol, 5.86 g) and acetophenone (25 mmol, 3.00 g) or 4-bromoacetophenone (25 mmol, 5.00 g) were dissolved in 350 mL of absolute ethanol saturated with hydrogen chloride gas; the resultant solution was then stirred for 2 h at room temperature and left overnight. Compound **1a** crystallized and was filtered off as a yellowish green crystal. Compound **1b** was obtained upon dilution with water. Purification of both **1a** and **1b** was carried out by recrystallization from ethanol. Yield: 80%, 6.5 g of **1a** and 81%, 6.6 g of **1b**.

^{1}H NMR of **1a** (500 MHz, 298 K, $CDCl_3$) δ (ppm) = 7.99−8.01 (d, *J* = 10 Hz, 2H), 7.76−7.79 (d, *J* = 15 Hz, 1H), 7.49−7.59 (m, 5H), 7.33−7.36 (d, *J* = 15 Hz, 1H), 5.57 (S, 1 H), 1.48 (S, 18H). ^{13}C NMR of **1a** (500 MHz, 298 K, $CDCl_3$) δ (ppm) = 30.2, 34.4, 119.3,126.0, 126.3, 128.45, 128.5, 132.4, 136.5, 138.8, 146.5, 156.6, 191.1.

^{1}H NMR of **1b** (500 MHz, 298 K, $CDCl_3$) δ (ppm) = 7.85−7.87 (d, *J* = 10 Hz, 2H), 7.75−7.78 (d, *J* = 15 Hz, 1H), 7.63−7.65 (d, *J* = 10 Hz, 2H), 7.48 (s, 2H), 7.27−7.30 (d, *J* = 15 Hz, 1H), 5.59 (S, 1 H), 1.48 (S, 18H). ^{13}C NMR of **1b** (500 MHz, 298 K, $CDCl_3$) δ (ppm) = 30.1, 34.4, 118.7, 126.1, 127.4, 130,131.8, 136.6, 137.5, 147.1, 156.8, 159.7, 189.9. HRMS (MALDI) of **1b** (*m/z*): $[M + H]^+$ calcd for $C_{23}H_{28}BrO_2$, 415.1273; found, 415.1265.

*Synthesis of 1-(3,5-Ditert-butyl-4-hydroxyphenyl)-4-nitro-3-phenylprop-2-en-1-one (**2a**) and 1-(4-Bromophenyl)-3-(3,5-ditert-butyl-4-hydroxyphenyl)-4-nitro-3-phenylbutan-1-one (**2b**).* To a solution of compound **1a** or **1b** (4.16 mmol, 1.4 g for **1a** and 4.74 mmol, 2.0 g for **1b**) in nitromethane (20 mL), 1,8-diazabicyclo[5.4.0]undec-7-ene (DBU) (4.16 mmol of DBU, 0.632g for **1a** or 4.74 mmol of DBU, 0.72 g for **1b**) was added. The resulting mixture was refluxed for 30 min. The resulting reddish-brown solution was cooled to room temperature and diluted with 2 mL 1% $HCl_{(aq)}$ and 30 mL of water. The product was extracted with chloroform and the organic layer was dried over $MgSO_4$ and evaporated to dryness, yielding 1.26 g (90% yield) of pure compound **2a** and 1.52 g (92% yield) of pure compound **2b**.

^{1}H NMR of **2a** (500 MHz, 298 K, $CDCl_3$) δ (ppm) = 7.88−7.90 (d, *J* = 10 Hz, 2H), 7.55−7.58 (t, 1H), 7.43−7.46 (t, 2H), 7.01 (s, 2H), 5.15 (s, 1H), 4.79−4.82 (m, 1H), 4.66−4.70 (m, 1H), 4.10−4.16 (m, 1H), 3.39−3.41 (m, 2H), 1.40 (s, 18H). ^{13}C NMR of **2a** (500 MHz, 298 K, $CDCl_3$) δ (ppm) = 30.4, 34.4, 39.5, 42.0, 79.8 123.6, 128.1, 128.7, 129.7, 133.4, 136.4, 153.2, 197.6. HRMS (MALDI) of **2a** (*m/z*): $[M + Na]^+$ calcd for $C_{24}H_{31}NO_4Na$, 420.2151; found, 420.2141.

^{1}H NMR of **2b** (500 MHz, 298 K, $CDCl_3$) δ (ppm) = 7.73−7.75 (d, *J* = 10 Hz, 2H), 7.57−7.59 (d, *J* = 10 Hz, 2H), 6.99 (s, 2H), 5.16 (s, 1H), 4.76−4.80 (m, 1H), 4.65−4.69 (m, 1H), 4.07−4.13 (m, 1H), 3.35−3.37 (m, 2H), 1.40 (s, 18H). ^{13}C NMR of **2b** (500 MHz, 298 K, $CDCl_3$) δ (ppm) = 30.3, 34.4, 39.5, 42.0, 79.7 123.9, 128.6, 129.6, 132, 135.4 136.4, 153.3, 196.6. HRMS (MALDI) of **2b** (*m/z*): $[M-H]^-$ calcd for $C_{24}H_{29}BrNO_4$, 474.1280; found, 474.1260.

*Synthesis of 2,6-Ditert-butyl-4-(2-((3-(3,5-ditert-butyl-4-hydroxyphenyl)-5-phenyl-1H-pyrrol-2-yl)imino)-5-phenyl-2H-pyrrol-3-yl)phenol (**3a**) and 4-(5-(4-Bromophenyl)-2-((5-(4-bromophenyl)-3-(3,5-ditert-butyl-4-hydroxyphenyl)-1H-pyrrol-2-yl)imino)-2H-pyrrol-3-yl)-2,6-ditert-butylphenol (**3b**).* A mixture of compound **2a** or **2b** (3.062 mmol, 1.26 g for **1a** or 3.062 mmol, 1.46 g for **1b**) and ammonium acetate (50 equiv) was refluxed in *n*-butanol (100 mL) for 36 h. After cooling to room temperature, the solvent concentrated to 30 mL and the precipitate was filtered off, washed with ethanol, and dried to yield compound **3a** or **3b** as a purplish blue solid (0.36 g of **3a,** 28% yield and 0.43 g of **3b**, 28% yield).

^{1}H NMR of **3a** (500 MHz, 298 K, $CDCl_3$) δ (ppm) = 7.95−7.97 (d, *J* = 10 Hz, 4H), 7.51−7.54 (t, 4H), 7.48 (s, 4 H), 7.43−7.46 (t, 2H), 7.01 (s, 2H), 5.25 (s, 2H), 1.32 (s, 36H) (NH not observed). ^{13}C NMR of **3a** (500 MHz, 298 K, $CDCl_3$) δ (ppm) = 30.4, 34.2, 114.0, 125.6, 126.5, 126.9, 129.1, 129.7. 132.7, 135.2, 145.2, 149.6, 154.1, 154.6. UV/vis of **3a** (CH_2Cl_2, λ_{max}[nm] (ε, 10^4 M^{-1} cm^{-1})): 592 (3.45). HRMS (ESI) of **3a** (*m/z*): $[M + H]^+$ calcd for $C_{48}H_{56}N_3O_2$, 706.4373; found, 706.4341.

^{1}H NMR of **3b** (500 MHz, 298 K, $CDCl_3$) δ (ppm) = 7.78−7.80 (d, *J* = 10 Hz, 4H), 7.64−7.66 (d, *J* = 10 Hz, 4H), 7.45 (s, 4 H), 6.96 (s, 2H), 5.27 (s, 2H), 1.31 (s, 36H) (NH not observed). ^{13}C NMR of **3b** (500 MHz, 298 K, $CDCl_3$) δ (ppm) = 30.4, 34.3, 114.0, 124.03, 125.4, 126.9, 127.8, 131.5, 132.3. 135.2, 145.6, 149.7, 153.7, 154.2. UV/vis of **3b** (CH_2Cl_2, λ_{max}[nm] (ε, 10^4 M^{-1} cm^{-1})): 600 (6.84). HRMS (MALDI) of **3b** (*m/z*): $[M + Na]^+$ calcd $C_{48}H_{53}Br_2N_3O_2Na$, 886.2388; found, 886.2376.

Compound **3a** was further characterized by single crystal X-ray analysis. The single crystals of **3a** were grown from butanol solution.

*Synthesis of BF_2Chelate of 2,6-Ditert-butyl-4-(2-((3-(3,5-ditert-butyl-4-hydroxyphenyl)-5-phenyl-1H-pyrrol-2-yl)imino)-5-phenyl-2H-pyrrol-3-yl)phenol (**4a**) and BF_2Chelate of 4-(5-(4-Bromophenyl)-2-((5-(4-bromophenyl)-3-(3,5-ditert-butyl-4-hydroxyphenyl)-1H-pyrrol-2-yl)imino)-2H-pyrrol-3-yl)-2,6-ditert-butylphenol (**4b**).* A solution of compound **3a** (0.26 mmol, 0.184 g) or **3b** (0.26 mmol, 0.225 g) was prepared in dry DCM (50 mL), treated with *N*,*N*-diisopropylethylamine (DIPEA) (1.28 mmol, 0.22 mL) and $BF_3\cdot Et_2O$ (1.80 mmol, 0.22 mL), and stirred at room temperature for 24 h under a nitrogen atmosphere. Then, the reaction mixture was washed with 50 mL of water, and the organic layer was dried over sodium sulfate and evaporated to dryness. Column chromatography on silica gel eluting with methylene chloride/hexane (1:1) gave the product as a blue solid (0.14 g of **4a**, 62% yield and 0.16 g of **4b**, 63% yield)

^{1}H NMR of **4a** (500 MHz, 298 K, $CDCl_3$) δ (ppm) = 8.01−8.03 (m, 4H), 7.60 (s, 4H), 7.45− 7.49 (m, 6H). 6.80 (s, 2H), 5.45 (s, 2H), 1.38 (s, 36H). ^{13}C NMR of **4a** (500 MHz, 298 K, $CDCl_3$) δ (ppm) = 30.4, 34.4, 118.5, 124.6, 127, 128.5, 129.4, 130.4, 132.1, 136.0, 145.9, 146.7, 155.4, 158.4. UV/vis of **4a** (CH_2Cl_2, λ_{max}[nm] (ε, 10^4 M^{-1} cm^{-1})): 658 (7.02). Fluorescence of **4a** ($CHCl_3$, λ_{em}[nm] (λ_{ex}[nm], Φ_F)): 706 (638, 0.19). HRMS (ESI) of **4a** (*m/z*): $[M + H]^+$ calcd for $C_{48}H_{55}BF_2N_3O_2$, 754.4363; found, 754.4341.

^{1}H NMR of **4b** (500 MHz, 298 K, $CDCl_3$) δ (ppm) = 7.88−7.90 (d, *J* = 10 Hz, 4H), 7.59− 7.61 (m, 8H). 6.78 (s, 2H), 5.48 (s, 2H), 1.37 (s, 36H). ^{13}C NMR of **4b** (500 MHz, 298 K, $CDCl_3$) δ (ppm) = 30.4, 34.4, 118.2, 124.4, 125.4, 127, 130.85, 130.92, 131.8, 136.1, 146.1, 147.1, 155.6, 157.1. UV/vis of **4b** (CH_2Cl_2, λ_{max}[nm] (ε, 10^4 M^{-1} cm^{-1})): 670 (5.87). Fluorescence of **4b** ($CHCl_3$, λ_{em}[nm] (λ_{ex}[nm], Φ_F)): 716 (650, 0.13). HRMS (MALDI) of **4b** (*m/z*): $[M]^+$ calcd for $C_{48}H_{52}BBr_2F_2N_3O_2$, 911.2480; found, 911.2482.

*Synthesis of 4,4′-(5,5-Difluoro-3,7-diphenyl-1H-$4\lambda^4$,$5\lambda^4$-dipyrrolo[1,2-c:2′,1′-f][1,3,5,2]triazaborinine-1,9(5H)-diylidene)bis(2,6-ditert-butylcyclohexa-2,5-dien-1-one) (**5a**) and 4,4′-(3,7-Bis(4-bromophenyl)-5,5-difluoro-1H-$4\lambda^4$,$5\lambda^4$-dipyrrolo[1,2-c:2′,1′-f][1,3,5,2]triazaborinine-1,9(5H)-diylidene)bis(2,6-ditert-butylcyclohexa-2,5-dien-1-one) (**5b**).* Dry DCM was added into a mixture of compound **4a** (75 mg, 0.1 mmol) or **4b** (91 mg, 0.1 mmol) and lead(II) oxide under argon (0.718 g, 3 mmol), and the reaction mixture was stirred at room temperature for half an hour with a color change from deep blue to greenish brown. The reaction was monitored by TLC. Once the reaction was finished, the solid lead(II) oxide was filtered off. The filtrate was dried via rotary evaporator, and then the final product was obtained as a black solid (73.5 mg of **5a**, 99% yield and 90 mg of **5b**, 99% yield) without further purification.

^{1}H NMR of **5a** (500 MHz, 298 K, THF-d_8) δ (ppm) = 9.00 (s, 2H), 7.84−7.86 (m, 4H), 7.66 (s, 2H), 7.36−7.40 (m, 6H), 6.91 (s, 2H), 1.32−1.37 (d, 36H). ^{13}C NMR of **5a** (500 MHz, 298 K, $CDCl_3$) δ (ppm) = 29.5, 36.32, 110, 128.2, 128.8, 129.2, 130, 131.8, 140.4, 141.1, 151.9, 152.7, 161.6, 186. UV/vis of **5a** (CH_2Cl_2, λ_{max}[nm] (ε, 10^4 M^{-1} cm^{-1})): 387 (7.55), 805 (2.70). HRMS (ESI) of **5a** (*m/z*): $[M + H]^+$ calcd for $[C_{48}H_{53}BF_2N_3O_2]$, 752.4107; found, 752.4176.

^{1}H NMR of **5b** (500 MHz, 298 K, DMF-d_7) δ (ppm) = 8.97 (s, 2H), 7.89−7.90 (d, 4H), 7.86 (s, 2H), 7.80−7.82 (d, 4H), 7.65 (s,

https://doi.org/10.1021/acs.inorgchem.4c04409
Inorg. Chem. 2024, 63, 24008−24021

2H), 1.28–1.32 (d, 36H). ^{13}C NMR of **5b** (500 MHz, 298 K, $CDCl_3$) δ (ppm) = 28.7, 35.4, 109.4, 123.7, 128.2, 129.7, 130, 130.7, 140, 150.5, 151.4, 152.1, 160.8, 185.8. UV/vis of **5b** (CH_2Cl_2, λ_{max}[nm] (ε, 10^4 M^{-1} cm^{-1})): 389 (5.69), 807 (2.26). HRMS (MALDI) of **5b** (*m*/*z*): $[M]^+$ calcd for $C_{48}H_{50}BBr_2F_2N_3O_2$, 909.2324.4363; found, 909.2349.

Compound **5a** was further characterized by single crystal X-ray analysis. The X-ray quality crystals of **5a** were grown by slow evaporation of the DMF solution.

■ ASSOCIATED CONTENT

Supporting Information

The Supporting Information is available free of charge at https://pubs.acs.org/doi/10.1021/acs.inorgchem.4c04409.

> ^{1}H and ^{13}C NMR spectra of new compounds, mass spectra of new compounds, electro- and spectroelectrochemistry of new compounds, IR spectra of **4a** and **5a**, additional variable-temperature ^{1}H NMR data, additional transient absorption spectroscopy data, additional magnetometry data, and DFT and TDDFT data (PDF)

Accession Codes

Deposition Numbers 2388285–2388288 contain the supplementary crystallographic data for this paper. These data can be obtained free of charge via the joint Cambridge Crystallographic Data Centre (CCDC) and Fachinformationszentrum Karlsruhe Access Structures service.

■ AUTHOR INFORMATION

Corresponding Authors

David A. Blank – *Department of Chemistry, University of Minnesota, Minneapolis, Minnesota 55455, United States;* orcid.org/0000-0003-2582-1537; Email: blank@umn.edu

Christopher J. Ziegler – *Department of Chemistry, University of Akron, Akron, Ohio 44325, United States;* orcid.org/0000-0002-0142-5161; Email: ziegler@uakron.edu

Victor N. Nemykin – *Department of Chemistry, University of Tennessee, Knoxville, Tennessee 37996, United States;* orcid.org/0000-0003-4345-0848; Email: vnemykin@utk.edu

Authors

Morris Oyelowo – *Department of Chemistry, University of Tennessee, Knoxville, Tennessee 37996, United States*

Jacob W. Schaffner – *Department of Chemistry, University of Minnesota, Minneapolis, Minnesota 55455, United States;* orcid.org/0000-0003-4970-3789

Towhidi Illius Jeaydi – *Department of Chemistry, University of Akron, Akron, Ohio 44325, United States*

Complete contact information is available at: https://pubs.acs.org/10.1021/acs.inorgchem.4c04409

Notes

The authors declare no competing financial interest.

■ ACKNOWLEDGMENTS

The generous computing time offered by the University of Minnesota Supercomputing Institute and support from NSF (CHE-2153081) to VNN is greatly appreciated. We also would like to thank Dr. P. Nalaoh for the help with the X-ray data collection.

■ REFERENCES

(1) Li, Y.; Jiang, M.; Yan, M.; Ye, J.; Li, Y.; Dehaen, W.; Yin, S. Near-infrared boron-dipyrrin (BODIPY) nanomaterials: Molecular design and anti-tumor therapeutics. *Coord. Chem. Rev.* **2024**, *506*, No. 215718.

(2) Ma, D.; Bian, H.; Gu, M.; Wang, L.; Chen, X.; Peng, X. Recent advances in the design and applications of near-infrared II responsive small molecule phototherapeutic agents. *Coord. Chem. Rev.* **2024**, *505*, No. 215677.

(3) Li, H.; Wang, J.; Jiao, L.; Hao, E. BODIPY-based photocages: rational design and their biomedical application. *Chem. Commun.* **2024**, *60*, 5770–5789.

(4) Kovtun, O. M.; Zatsikha, Y. V.; Kovtun, Y. P. New approaches to the modification of chemical structure and photophysical properties of BODIPY dyes. *Chem. Heterocycl. Compd.* **2023**, *59*, 357–367.

(5) Gapare, R. L.; Thompson, A. Substitution at boron in BODIPYs. *Chem. Commun.* **2022**, *58*, 7351–7359.

(6) Zatsikha, Y. V.; Prasannan, D.; Scharge, B.; Herbert, D. E.; Gerasimchuk, N. N.; Zeller, M.; Nemykin, V. N. Use of unprecedented intramolecular 1, 3-dipolar cycloaddition reaction in meso-nitrile oxide-containing BODIPYs as a new pathway for the preparation of fused NIR platforms. *Chem.—Eur. J.* **2024**, *30*, No. e202401210.

(7) Zatsikha, Y. V.; Blesener, T. S.; King, A. J.; Healy, A. T.; Goff, P. C.; Didukh, N. O.; Blank, D. A.; Kovtun, Y. P.; Nemykin, V. N. Fully conjugated pyrene-BODIPY and pyrene-BODIPY-ferrocene dyads and triads: synthesis, characterization, and selective noncovalent interactions with nanocarbon materials. *J. Phys. Chem. B* **2021**, *125*, 360–371.

(8) Zatsikha, Y. V.; Didukh, N. O.; Swedin, R. K.; Yakubovskyi, V. P.; Blesener, T. S.; Healy, A. T.; Herbert, D. E.; Blank, D. A.; Nemykin, V. N.; Kovtun, Y. P. Preparation of viscosity-sensitive isoxazoline/isoxazolyl-based molecular rotors and directly linked BODIPY-fulleroisoxazoline from the stable meso-(nitrile oxide)-substituted BODIPY. *Org. Lett.* **2019**, *21*, 5713–5718.

(9) Didukh, N. O.; Yakubovskyi, V. P.; Zatsikha, Y. V.; Rohde, G. T.; Nemykin, V. N.; Kovtun, Y. P. Flexible BODIPY platform that offers an unexpected regioselective heterocyclization reaction toward preparation of 2-pyridone[a]-fused BODIPYs. *J. Org. Chem.* **2019**, *84*, 2133–2147.

(10) Nemykin, V. N.; Blesener, T. S.; Ziegler, C. J. Photophysics, redox processes, and electronic structures of ferrocenyl-containing BODIPYs, aza-BODIPYs, BOPHYs, transition-metal dipyrromethenes and aza-dipyrromethenes. *Makrogeterotsikly* **2017**, *10*, 9–26.

(11) Didukh, N. O.; Zatsikha, Y. V.; Rohde, G. T.; Blesener, T. S.; Yakubovskyi, V. P.; Kovtun, Y. P.; Nemykin, V. N. NIR absorbing diferrocene-containing meso-cyano-BODIPY with a UV-Vis-NIR spectrum remarkably close to that of magnesium tetracyanotetraferrocenyltetraazaporphyrin. *Chem. Commun.* **2016**, *52*, 11563–11566.

(12) Shamova, L. I.; Zatsikha, Y. V.; Nemykin, V. N. Synthesis pathways for the preparation of the BODIPY analogues: aza-BODIPYs, BOPHYs and some other pyrrole-based acyclic chromophores. *Dalton Trans.* **2021**, *50*, 1569–1593.

(13) Wang, J.; Yu, C.; Hao, E.; Jiao, L. Conformationally restricted and ring-fused aza-BODIPYs as promising near infrared absorbing and emitting dyes. *Coord. Chem. Rev.* **2022**, *470*, No. 214709.

(14) Kaur, M.; Janaagal, A.; Balsukuri, N.; Gupta, I. Evolution of aza-BODIPY dyes-A hot topic. *Coord. Chem. Rev.* **2024**, *498*, No. 215428.

(15) Zatsikha, Y. V.; Blesener, T. S.; Goff, P. C.; Healy, A. T.; Swedin, R. K.; Herbert, D. E.; Rohde, G. T.; Chanawanno, K.; Ziegler, C. J.; Belosludov, R. V.; Blank, D. A.; Nemykin, V. N. 1,7-dipyrene-containing aza-BODIPYs: Are pyrene groups effective as ligands to promote and direct complex formation with common nanocarbon materials? *J. Phys. Chem. C* **2018**, *122*, 27893–27916.

(16) Zatsikha, Y. V.; Holstrom, C. D.; Chanawanno, K.; Osinski, A. J.; Ziegler, C. J.; Nemykin, V. N. Observation of the strong electronic coupling in near-infrared-absorbing tetraferrocene aza-dipyrromethene and aza-BODIPY with direct ferrocene-α- and ferrocene-β-

pyrrole bonds: toward molecular machinery with four-bit information storage capacity. *Inorg. Chem.* **2017**, *56*, 991−1000.

(17) Maligaspe, E.; Pundsack, T. J.; Albert, L. M.; Zatsikha, Y. V.; Solntsev, P. V.; Blank, D. A.; Nemykin, V. N. Synthesis and Charge-transfer dynamics in a ferrocene-containing organoboryl aza-BODIPY donor-acceptor triad with boron as the hub. *Inorg. Chem.* **2015**, *54*, 4167−4174.

(18) Wang, J.; Gong, Q.; Jiao, L.; Hao, E. Research advances in BODIPY-assembled supramolecular photosensitizers for photodynamic therapy. *Coord. Chem. Rev.* **2023**, *496*, No. 215367.

(19) Mahanta, C. S.; Ravichandiran, V.; Swain, S. P. Recent developments in the design of new water-soluble boron dipyrromethenes and their applications: An updated review. *ACS Appl. Bio Mater.* **2023**, *6*, 2995−3018.

(20) Vargas-Zuniga, G. I.; Kim, H. S.; Li, M.; Sessler, J. L.; Kim, J. S. Pyrrole-based photosensitizers for photodynamic therapy - a Thomas Dougherty award (for excellence in PDT) paper. *J. Porphyrins Phthalocyanines* **2021**, *25*, 773−793.

(21) Wang, J.; Gong, Q.; Wang, L.; Hao, E.; Jiao, L. The main strategies for tuning BODIPY fluorophores into photosensitizers. *J. Porphyrins Phthalocyanines* **2020**, *24*, 603−635.

(22) Kamkaew, A.; Lim, S. H.; Lee, H. B.; Kiew, L. V.; Chung, L. Y.; Burgess, K. BODIPY dyes in photodynamic therapy. *Chem. Soc. Rev.* **2013**, *42*, 77−88.

(23) Carmo, C.; Almeida, J. M. S.; Araujo, J.; Brett, C. M. A.; Botelho, M. F.; Cordova, A.; Laranjo, M.; Sobral, A. J. F. N. Exploring the impact of meso-position fluorination on BODIPYs: Synthesis, electrochemical Insights, and potential therapeutic applications in breast cancer. *Dyes Pigments* **2024**, *229*, No. 112263.

(24) Saladin, L.; Breton, V.; Le Berruyer, V.; Nazac, P.; Lequeu, T.; Didier, P.; Danglot, L.; Collot, M. Targeted photoconvertible BODIPYs based on directed photooxidation-induced conversion for applications in photoconversion and live super-resolution imaging. *J. Am. Chem. Soc.* **2024**, *146*, 17456−17473.

(25) Reese, A. E.; de Moliner, F.; Mendive-Tapia, L.; Benson, S.; Kuru, E.; Bridge, T.; Richards, J.; Rittichier, J.; Kitamura, T.; Sachdeva, A.; et al. Inserting ″OFF-to-ON″ BODIPY tags into cytokines: A fluorogenic interleukin IL-33 for real-time imaging of immune cells. *ACS Central Sci.* **2024**, *10*, 143−154.

(26) Zhang, Y.; Zheng, Y.; Tomassini, A.; Singh, A. K.; Raymo, F. M. Photoactivatable BODIPYs for live-cell PALM. *Molecules* **2023**, *28*, 2447.

(27) Gao, Y.; Pan, Y.; Chi, Y.; He, Y.; Chen, H.; Nemykin, V. N. A ″reactive″ turn-on fluorescence probe for hypochlorous acid and its bioimaging application. *Spectrochim. Acta, Part A* **2019**, *206*, 190−196.

(28) Yadav, I. S.; Misra, R. Design, synthesis and functionalization of BODIPY dyes: applications in dye-sensitized solar cells (DSSCs) and photodynamic therapy (PDT). *J. Mater. Chem. C* **2023**, *11*, 8688−8723.

(29) Knoll, S.; Zens, C.; Maisuradze, T.; Schmidt, H.; Kupfer, S.; Zedler, L.; Dietzek-Ivansic, B.; Streb, C. Light-induced charge separation in covalently linked BODIPY-quinone-alkyne dyads. *Chem.—Eur. J.* **2024**, *30*, No. e202303250.

(30) Ptaszek, M.; Meares, A.; Ansteatt, S. Hydroporphyrin-BODIPY arrays. *J. Porphyrins Phthalocyanines* **2024**, *28*, 201−216.

(31) Klfout, H.; Stewart, A.; Elkhalifa, M.; He, H. BODIPYs for dye-sensitized solar cells. *ACS Appl. Mater. Interfaces* **2017**, *9*, 39873−39889.

(32) Bucher, L.; Desbois, N.; Harvey, P. D.; Sharma, G. D.; Gros, C. P. Porphyrins and BODIPY as building blocks for efficient donor materials in bulk heterojunction solar cells. *Sol. RRL* **2017**, *1*, No. 1700127.

(33) Wu, D.; Zhang, Z.; Li, X.; Zhou, J.; Cao, Y.; Qi, S.; Wang, L.; Liu, Z.; Yu, G. Dynamically assembled nanomedicine based on host-guest molecular recognition for NIR laser-excited chemotherapy and phototheranostics. *Acta Biomater.* **2023**, *168*, 565−579.

(34) Chen, X.; Yu, B.; Wang, J.; Luo, Z.; Meng, H.; Xie, B.; Zhou, R.; Liu, S.; Zhao, Q. A near-infrared organic photodetector based on an aza-BODIPY dye for a laser microphone system. *J. Mater. Chem. C* **2023**, *11*, 2267−2272.

(35) Song, S.; Xu, G.; Yang, N.; Shahzad, S. A.; Lv, J.; Shen, X.; Yu, C. Aza-BODIPY nanoparticles for near-infrared triggered synergistic photothermal and photodynamic antibacterial therapy. *J. Mater. Sci.* **2022**, *57*, 21206−21218.

(36) Wu, Q.; Zhu, Y.; Fang, X.; Hao, X.; Jiao, L.; Hao, E.; Zhang, W. Conjugated BODIPY Oligomers with controllable near-infrared absorptions as promising phototheranostic agents through excited-state intramolecular rotations. *ACS Appl. Mater. Interfaces* **2020**, *12*, 47208−47219.

(37) Xu, Y.; Feng, T.; Yang, T.; Wei, H.; Yang, H.; Li, G.; Zhao, M.; Liu, S.; Huang, W.; Zhao, Q. Utilizing intramolecular photoinduced electron transfer to enhance photothermal tumor treatment of aza-BODIPY-based near-infrared nanoparticles. *ACS Appl. Mater. Interfaces* **2018**, *10*, 16299−16307.

(38) Pinjari, D.; Patil, Y.; Misra, R. Near-infrared absorbing aza-BODIPY Dyes for optoelectronic applications. *Chem.—Asian J.* **2024**, *19*, No. e202400167.

(39) Patil, Y.; Butenschon, H.; Misra, R. Tetracyanobutadiene bridged push-pull chromophores: Development of new generation optoelectronic materials. *Chem. Rec.* **2023**, *23*, No. e202200208.

(40) Squeo, B. M.; Ganzer, L.; Virgili, T.; Pasini, M. BODIPY-based molecules, a platform for photonic and solar cells. *Molecules* **2021**, *26*, 153.

(41) Poddar, M.; Misra, R. Recent advances of BODIPY based derivatives for optoelectronic applications. *Coord. Chem. Rev.* **2020**, *421*, No. 213462.

(42) Singh, S. P.; Gayathri, T. Evolution of BODIPY dyes as potential sensitizers for dye-sensitized solar cells. *Eur. J. Org. Chem.* **2014**, *2014*, 4689−4707.

(43) El-Khouly, M. E.; Fukuzumi, S.; D'Souza, F. Photosynthetic antenna-reaction center mimicry by using boron dipyrromethene sensitizers. *ChemPhysChem* **2014**, *15*, 30−47.

(44) Benniston, A. C.; Copley, G. Lighting the way ahead with boron dipyrromethene (Bodipy) dyes. *Phys. Chem. Chem. Phys.* **2009**, *11*, 4124−4131.

(45) Emilio de la Cerda-Pedro, J.; Hernandez-Ortiz, O. J.; Vazquez-Garcia, R. A.; Garcia-Baez, E. V.; Gomez-Aguilar, R.; Espinosa-Roa, A.; Farfan, N.; Padilla-Martinez, I. I. Highly crystalline and fluorescent BODIPY-labelled phenyl-triazole-coumarins as n-type semiconducting materials for OFET devices. *Heliyon* **2024**, *10*, No. e23517.

(46) Talalaev, F. S.; Frolova, L. A.; Bochkov, A. Y.; Babenko, S. D.; Gutsev, L. G.; Aldoshin, S. M.; Traven, V. F.; Troshin, P. A. Efficient OFET-based optical memory and photodetectors using novel BODIPY dye. *J. Mater. Chem. C* **2023**, *11*, 742−749.

(47) Ozcan, E.; Ozdemir, M.; Ho, D.; Zorlu, Y.; Ozdemir, R.; Kim, C.; Usta, H.; Cosut, B. A solution-processable meso-phenyl-BODIPY-based n-channel semiconductor with enhanced fluorescence emission. *ChemPlusChem.* **2019**, *84*, 1423−1431.

(48) Huaulme, Q.; Sutter, A.; Fall, S.; Jacquemin, D.; Leveque, P.; Retailleau, P.; Ulrich, G.; Leclerc, N. Versatile synthesis of α-fused BODIPY displaying intense absorption in the NIR region and high electron affinity. *J. Mater. Chem. C* **2018**, *6*, 9925−9931.

(49) Ozdemir, M.; Choi, D.; Zorlu, Y.; Cosut, B.; Kim, H.; Kim, C.; Usta, H. A new rod-shaped BODIPY-acetylene molecule for solution-processed semiconducting microribbons in n-channel organic field-effect transistors. *New J. Chem.* **2017**, *41*, 6232−6240.

(50) Gawale, Y.; Palanisamy, P.; Lee, H. S.; Chandra, A.; Kim, H. U.; Ansari, R.; Chae, M. Y.; Kwon, J. H. Structural optimization of BODIPY derivatives: Achieving stable and long-lived green emission in hyperfluorescent OLEDs. *ACS Appl. Mater. Interfaces* **2024**, *16*, 22274−22281.

(51) Jiang, W.; Zhou, R.; Zhao, G.; Ma, D.; Chen, H.; Zhang, Z.; Tian, W.; Sun, Y. Isomer engineering to adjusting full width at half maximum and emission wavelength for efficient solution-processed red OLEDs. *Optical Mater.* **2023**, *136*, No. 113505.

(52) Liu, J.; Liu, J.; Li, H.; Bin, Z.; You, J. Boron-dipyrromethene-based fluorescent emitters enable high-performance narrowband red

organic light-emitting diodes. *Angew. Chem., Int. Ed.* **2023**, *62*, No. e202306471.

(53) Ma, D.; Zhao, G.; Chen, H.; Zhou, R.; Zhang, G.; Tian, W.; Jiang, W.; Sun, Y. Creation of BODIPYs-based red OLEDs with high color purity via modulating the energy gap and restricting rotation of substituents. *Dyes Pigments* **2022**, *203*, No. 110377.

(54) Jung, Y. H.; Karthik, D.; Lee, H.; Maeng, J. H.; Yang, K. J.; Hwang, S.; Kwon, J. H. A new BODIPY material for pure color and long lifetime red hyperfluorescence organic light-emitting diode. *ACS Appl. Mater. Interfaces* **2021**, *13*, 17882−17891.

(55) Ivaniuk, K.; Pidluzhna, A.; Stakhira, P.; Baryshnikov, G. V.; Kovtun, Y. P.; Hotra, Z.; Minaev, B. F.; Agren, H. BODIPY-core 1,7-diphenyl-substituted derivatives for photovoltaics and OLED applications. *Dyes Pigments* **2020**, *175*, No. 108123.

(56) *Diradicaloids*, Wu, J., Ed.; Jenny Stanford Publishing, 2022; pp 1−622.

(57) Zeng, Z.; Shi, X.; Chi, C.; Lopez Navarrete, J. T.; Casado, J.; Wu, J. Pro-aromatic and anti-aromatic π-conjugated molecules: an irresistible wish to be diradicals. *Chem. Soc. Rev.* **2015**, *44*, 6578−6596.

(58) Olivier, Y.; Sancho-Garcia, J.-C. Design strategies for diradical boron/nitrogen doped carbon-based materials. *Angew. Chem., Int. Ed.* **2023**, *62*, No. e202305501.

(59) Moles Quintero, S.; Haley, M. M.; Kertesz, M.; Casado, J. Polycyclic hydrocarbons from [4n]Annulenes: Correlation versus hybridization forces in the formation of diradicaloids. *Angew. Chem., Int. Ed.* **2022**, *61*, No. e202209138.

(60) Kato, S.-I. Phenanthrylene-alkynylene macrocycles, phenanthrene-fused dicyclopenta[b,g]naphthalene, as well as relevant diradicaloids and antiaromatic compounds. *Adv. Phys. Org. Chem.* **2021**, *55*, 41−66.

(61) Dressler, J. J.; Haley, M. M. Learning how to fine-tune diradical properties by structure refinement. *J. Phys. Org. Chem.* **2020**, *33*, No. e4114.

(62) Stuyver, T.; Chen, B.; Zeng, T.; Geerlings, P.; De Proft, F.; Hoffmann, R. Do diradicals behave like radicals? *Chem. Rev.* **2019**, *119*, 11291−11351.

(63) Liu, C.; Ni, Y.; Lu, X.; Li, G.; Wu, J. Global aromaticity in macrocyclic polyradicaloids: Hückel's rule or baird's rule? *Acc. Chem. Res.* **2019**, *52*, 2309−2321.

(64) Kirk, M. L.; Shultz, D. A.; Marri, A.; Reddy; van der Est, A. Photoinduced magnetic exchange-jump promotes ground state biradical electron spin polarization. *J. Am. Chem. Soc.* **2024**, *146*, 9285−9292.

(65) Miller, P. D.; Mengell, J.; Shultz, D. A.; Kirk, M. L. Metal-ligand exchange coupling alters the open-shell ligand electronic structure in a bis(semiquinone) complex. *Inorg. Chem.* **2024**, *63*, 6493−6499.

(66) Banachowicz, P.; Das, M.; Kruczala, K.; Siczek, M.; Sojka, Z.; Kijewska, M.; Pawlicki, M. Breaking global diatropic current to tame diradicaloid character: Thiele's hydrocarbon under macrocyclic constraints. *Angew. Chem., Int. Ed.* **2024**, *63*, No. e202400780.

(67) Maiti, A.; Elvers, B. J.; Bera, S.; Lindl, F.; Krummenacher, I.; Ghosh, P.; Braunschweig, H.; Yildiz, C. B.; Schulzke, C.; Jana, A. Disclosing cyclic(alkyl)(amino)carbenes as one-electron reductants: synthesis of acyclic(amino)(aryl)carbene-based Kekule diradicaloids. *Chem.—Eur. J.* **2022**, *28*, No. e202104567.

(68) Yamamoto, K.; Quintero, S. M.; Jinnai, S.; Jeong, E.; Matsuo, K.; Suzuki, M.; Yamada, H.; Casado, J.; Ie, Y. Cross-conjugated isothianaphthene quinoids: a versatile strategy for controlling electronic structures. *J. Mater. Chem. C* **2022**, *10*, 4424−4433.

(69) Maiti, A.; Sobottka, S.; Chandra, S.; Jana, D.; Ravat, P.; Sarkar, B.; Jana, A. Diamidocarbene-based Thiele and Tschitschibabin hydrocarbons: Carbonyl functionalized Kekulé diradicaloids. *J. Org. Chem.* **2021**, *86*, 16464−16472.

(70) Maiti, A.; Chandra, S.; Sarkar, B.; Jana, A. Acyclic diaminocarbene-based Thiele, Chichibabin, and Muller hydrocarbons. *Chem. Sci.* **2020**, *11*, 11827−11833.

(71) Kundu, G.; De, S.; Tothadi, S.; Das, A.; Koley, D.; Sen, S. S. Saturated N-heterocyclic carbene based Thiele's Hydrocarbon with a tetrafluorophenylene linker. *Chem.—Eur. J.* **2019**, *25*, 16533−16537.

(72) Hansmann, M. M.; Melaimi, M.; Munz, D.; Bertrand, G. Modular approach to Kekule diradicaloids derived from cyclic (alkyl)(amino)carbenes. *J. Am. Chem. Soc.* **2018**, *140*, 2546−2554.

(73) Rottschaefer, D.; Neumann, B.; Stammler, H.-G.; Andrada, D. M.; Ghadwal, R. S. Kekule diradicaloids derived from a classical N-heterocyclic carbene. *Chem. Sci.* **2018**, *9*, 4970−4976.

(74) Takamuku, S.; Nakano, M.; Kertesz, M. Intramolecular pancake bonding in helical structures. *Chem.—Eur. J.* **2017**, *23*, 7474−7482.

(75) Mishra, S.; Melidonie, J.; Eimre, K.; Obermann, S.; Groning, O.; Pignedoli, C. A.; Ruffieux, P.; Feng, X.; Fasel, R. On-surface synthesis of super-heptazethrene. *Chem. Commun.* **2020**, *56*, 7467−7470.

(76) Maeda, T.; Oka, T.; Sakamaki, D.; Fujiwara, H.; Suzuki, N.; Yagi, S.; Konishi, T.; Kamada, K. Unveiling a new aspect of oxocarbons: open-shell character of 4- and 5-membered oxocarbon derivatives showing near-infrared absorption. *Chem. Sci.* **2023**, *14*, 1978−1985.

(77) Sugiura, S.; Kubo, T.; Haketa, Y.; Hori, Y.; Shigeta, Y.; Sakai, H.; Hasobe, T.; Maeda, H. Deprotonation-induced and ion-pairing-modulated diradical properties of partially conjugated pyrrole-quinone conjunction. *J. Am. Chem. Soc.* **2023**, *145*, 8122−8129.

(78) Li, G.; Phan, H.; Herng, T. S.; Gopalakrishna, T. Y.; Liu, C.; Zeng, W.; Ding, J.; Wu, J. Toward stable superbenzoquinone diradicaloids. *Angew. Chem., Int. Ed.* **2017**, *56*, 5012−5016.

(79) Matsuta, Y.; Sakamaki, D.; Kurata, R.; Ito, A.; Seki, S. Modulation of open-shell characters of amine-inserted diphenoquinones via structural modification. *Chem.—Asian J.* **2017**, *12*, 1889−1894.

(80) Zhou, J.; Rieker, A. Electrochemical and spectroscopic properties of a series of tert-butyl-substituted para-extended quinones. *J. Chem. Soc., Perkin Trans.* **1997**, *2*, 931−938.

(81) Rebmann, A.; Zhou, J.; Schuler, P.; Stegmann, H. B.; Rieker, A. Synthesis, EPR spectroscopy and voltammetry of a p-quaterphenyl biradical/quinone. *J. Chem. Res., Synop.* **1996**, 318−319.

(82) Traylor, T. G.; Nolan, K. B.; Hildreth, R. Polyvalent porphyrins. 1. Properties of tetrakis(3,5-di-tert-butyl-4-hydroxyphenyl)porphyrin (1-P) and its iron(III) and zinc(II) derivatives. *J. Am. Chem. Soc.* **1983**, *105*, 6149−6151.

(83) Hill, J. P.; Hewitt, I. J.; Anson, C. E.; Powell, A. K.; McCarty, A. L.; Karr, P. A.; Zandler, M. E.; D'Souza, F. Highly nonplanar, electron deficient, N-substituted tetra-oxocyclohexadienylidene porphyrinogens: Structural, computational, and electrochemical investigations. *J. Org. Chem.* **2004**, *69*, 5861−5869.

(84) Ding, Y.; Li, X.; Hill, J. P.; Ariga, K.; Agren, H.; Andreasson, J.; Zhu, W.; Tian, H.; Xie, Y. Acid/Base switching of the tautomerism and conformation of a dioxoporphyrin for integrated binary subtraction. *Chem.—Eur. J.* **2014**, *20*, 12910−12916.

(85) Miao, F.; Phan, H.; Wu, J. A BODIPY-bridged bisphenoxyl diradicaloid: solvent-dependent diradical character and physical properties. *Molecules* **2019**, *24*, 1446.

(86) Pivovarenko, V. G.; Klymchenko, A. S. Fluorescent probes based on charge and proton transfer for probing biomolecular environment. *Chem. Rec.* **2024**, *24*, No. e202300321.

(87) Fontes, L. F. B.; Rocha, J.; Silva, A. M. S.; Guieu, S. Excited-state proton transfer in luminescent dyes: From theoretical insight to experimental evidence. *Chem.—Eur. J.* **2023**, *29*, No. e202301540.

(88) Kosower, E. M.; Huppert, D. Excited state electron and proton transfers. *Annu. Rev. Phys. Chem.* **1986**, *37*, 127−156.

(89) Robin, M. B.; Day, P. Mixed-valence chemistry: A survey and classification. *Adv. Inorg. Chem. Radiochem.* **1968**, *10*, 247−422.

(90) *Electron paramagnetic resonance; A practitioner's toolkit*, Brustolon, M.; Giamello, E., Eds.; Wiley, 2009; p 539.

(91) Nakano, M. Open-shell-character-based molecular design principles: Applications to nonlinear optics and singlet fission. *Chem. Rec.* **2017**, *17*, 27−62.

(92) Nakano, M.; Kishi, R.; Ohta, S.; Takahashi, H.; Kubo, T.; Kamada, K.; Ohta, K.; Botek, E.; Champagne, B. Relationship between third-order nonlinear optical properties and magnetic interactions in open-shell systems: A new paradigm for nonlinear optics. *Phys. Rev. Lett.* **2007**, *99*, No. 033001.

(93) Zatsikha, Y. V.; Shamova, L. I.; Blesener, T. S.; Kuzmin, I. A.; Germanov, Y. V.; Herbert, D. E.; Nemykin, V. N. Development of a class of easily scalable, electron-deficient, core-extended benzo-fused azadipyrromethene derivatives ("MB-DIPY"). *J. Org. Chem.* **2019**, *84*, 14540−14557.

(94) Zatsikha, Y. V.; Shamova, L. I.; Blesener, T. S.; Herbert, D. E.; Nemykin, V. N. Rigid, yet flexible: formation of unprecedented silver MB-DIPY dimers with orthogonal chromophore geometry. *Dalton Trans.* **2020**, *49*, 5034−5038.

(95) Zatsikha, Y. V.; Shamova, L. I.; Schaffner, J. W.; Healy, A. T.; Blesener, T. S.; Cohen, G.; Wozniak, B.; Blank, D. A.; Nemykin, V. N. Probing electronic communication and excited-State dynamics in the unprecedented ferrocene-containing zinc MB-DIPY. *ACS Omega* **2020**, *5*, 28656−28662.

(96) Zatsikha, Y. V.; Shamova, L. I.; Shepit, M.; Berry, S. M.; Thomas, F.; Herbert, D. E.; van Lierop, J.; Nemykin, V. N. Radical Complexes of nickel(II)/copper(II) and redox non-innocent MB-DIPY ligands: Unusual stability and strong near-infrared absorption at λmax ∼ 1300 nm. *Chem.—Eur. J.* **2022**, *28*, No. e202201181.

(97) *KaleidaGraph, version 5.04*, 1986−2023; Synergy Software Inc.

(98) Sheldrick, G. M. A short history of *SHELX*. *Acta Crystallogr.* **2008**, *A64*, 112−122.

(99) *Bruker-AXS APEX3 v2016.1−0*, Madison, Wisconsin, USA, 2016.

(100) Spek, A. L. Structure validation in chemical crystallography. *Acta Crystallogr.* **2009**, *D65*, 148−155.

(101) Macrae, C. F.; Sovago, I.; Cottrell, S. J.; Galek, P. T. A.; McCabe, P.; Pidcock, E.; Platings, M.; Shields, G. P.; Stevens, J. S.; Towler, M.; Wood, P. A. Mercury 4.0: from visualization to analysis, design and prediction. *J. Appl. Crystallogr.* **2020**, *53*, 226−235.

(102) Frisch, M. J.; Trucks, G. W.; Schlegel, H. B.; Scuseria, G. E.; Robb, M. A.; Cheeseman, J. R.; Scalmani, G.; Barone, V.; Petersson, G. A.; Nakatsuji, H.; Li, X.; Caricato, M.; Marenich, A. V.; Bloino, J.; Janesko, B. G.; Gomperts, R.; Mennucci, B.; Hratchian, H. P.; Ortiz, J. V.; Izmaylov, A. F.; Sonnenberg, J. L.; Williams-Young, D.; Ding, F.; Lipparini, F.; Egidi, F.; Goings, J.; Peng, B.; Petrone, A.; Henderson, T.; Ranasinghe, D.; Zakrzewski, V. G.; Gao, J.; Rega, N.; Zheng, G.; Liang, W.; Hada, M.; Ehara, M.; Toyota, K.; Fukuda, R.; Hasegawa, J.; Ishida, M.; Nakajima, T.; Honda, Y.; Kitao, O.; Nakai, H.; Vreven, T.; Throssell, K.; Montgomery, J. A., Jr.; Peralta, J. E.; Ogliaro, F.; Bearpark, M. J.; Heyd, J. J.; Brothers, E. N.; Kudin, K. N.; Staroverov, V. N.; Keith, T. A.; Kobayashi, R.; Normand, J.; Raghavachari, K.; Rendell, A. P.; Burant, J. C.; Iyengar, S. S.; Tomasi, J.; Cossi, M.; Millam, J. M.; Klene, M.; Adamo, C.; Cammi, R.; Ochterski, J. W.; Martin, R. L.; Morokuma, K.; Farkas, O.; Foresman, J. B.; Fox, D. J. *Gaussian 16, Revision B.01*; Gaussian, Inc.: Wallingford CT, 2016.

(103) Tenderholt, A. L. *QMForge, version 2.1*; Standord University: Stanford, CA, 2011. https://qmforge.net/.

(104) Tao, J. M.; Perdew, J. P.; Staroverov, V. N.; Scuseria, G. E. Climbing the density functional ladder: Nonempirical meta-generalized gradient approximation designed for molecules and solids. *Phys. Rev. Lett.* **2003**, *91*, 146401/1−146401/4.

(105) Staroverov, V. N.; Scuseria, G. N.; Tao, J.; Perdew, J. P. Comparative assessment of a new nonempirical density functional: Molecules and hydrogen-bonded complexes. *J. Chem. Phys.* **2003**, *119*, 12129−12137.

(106) Zhao, Y.; Truhlar, D. G. The M06 Suite of density functionals for main group thermochemistry, thermochemical kinetics, non-covalent interactions, excited states, and transition elements: Two new functionals and systematic testing of four M06 functionals and twelve other functionals. *Theor. Chem. Acc.* **2008**, *120*, 215−241.

(107) Becke, A. D. Density-functional thermochemistry. III. The role of exact exchange. *J. Chem. Phys.* **1993**, *98*, 5648−5652.

(108) Chai, J. D.; Head-Gordon, M. Long-range corrected hybrid density functionals with damped atom-atom dispersion corrections. *Phys. Chem. Chem. Phys.* **2008**, *10*, 6615−6620.

(109) McLean, A. D.; Chandler, G. S. Contracted Gaussian basis sets for molecular calculations. 1. Second row atoms, Z = 11−18. *J. Chem. Phys.* **1980**, *72*, 5639−5648.

(110) Herdan, J. M.; Dinoiu, V.; Meghea, A.; Schiketanz, A.; Gheorghiu, M. D.; Balaban, A. T. Synthesis and EPR spectra of persistent aroxyls. Part 5. AROXYLS derived from chalcone and derivatives. *Rev. Roumaine Chim.* **1990**, *35*, 1017−1024.